PERSPECTIVE

Check for updates

Solid oxide proton conductors beyond perovskites

Sacha Fop (ID) *[ab]

Solid oxide proton conductors are crucially emerging as key materials for enabling hydrogen-based energy conversion, storage, and electrochemical technologies. Oxides crystallising in the ideal ABO_3 perovskite structure, such as barium cerates and zirconates, are widely investigated thanks to their excellent proton conducting properties. Nevertheless, alternative structure-type solid oxide systems (hexagonal perovskite derivatives, brownmillerite, scheelite, *etc.*) can efficiently incorporate and enable the transport of protonic defects, with recent reports of materials exhibiting high ionic conductivity comparable to the conventional perovskite conductors. This perspective provides an overview of these alternative and less established proton conducting materials, with particular attention to the relationship between the structural and ionic conduction features and the mechanistic aspects. The goals are to highlight the differences between these materials and the traditional perovskites and to point out new potential crystal routes for the discovery of innovative solid oxide proton conductors.

1. Introduction

Carbon emissions must be reduced to mitigate the effects of climate change and keep the global average temperature increase below 2 °C above pre-industrial levels. To achieve this target, it is essential to transition away from fossil fuels and progress towards cleaner and renewable means of energy generation. Low carbon solutions provided by hydrogen-based

[a]*ISIS Facility, Rutherford Appleton Laboratory, Harwell, OX11 0QX, UK. E-mail: sacha.fop@stfc.ac.uk*

[b]*The Chemistry Department, University of Aberdeen, Meston Walk, Aberdeen AB24 3UE, UK*

Sacha Fop is Instrument Scientist on the High Resolution Powder Diffractometer (HRPD) at the ISIS Neutron and Muon Source, and Honorary Research Fellow in the School of Natural and Computing Sciences of the University of Aberdeen. Sacha obtained his BSc and MSc in Chemistry from the University of Perugia, Italy. He received his PhD from the University of Aberdeen (under the supervision of Professor Abbie Mclaughlin), where he also spent three years as a Postdoctoral Research Fellow. His research focuses on the design and discovery of novel solid-state ionic conductors for energy-related applications and in the characterisation of their structure–property relationships.
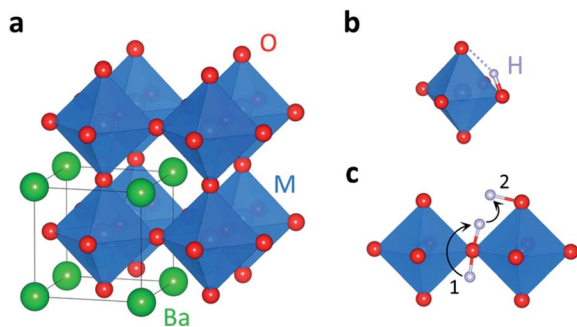
energy conversion, storage and electrochemical technologies will have a fundamental role in contributing to broad decarbonisation.[1,2] Conventional solid-state hydrogen-based electrochemical devices such as ceramic fuel cells and electrolysers employ oxide ion conducting materials. These systems however generally show adequate ionic conductivities only at high working temperatures (>700 °C), thus posing technical challenges in terms of materials selection and durability and limiting the widespread application of these technologies.[3-7] Systems based on solid oxide proton conductors offer promise of operations at reduced temperatures, thanks to the generally lower activation energy for proton diffusion ($\sim$0.3–0.6 eV) compared to oxide ion conduction in oxides ($\sim$0.6–1.2 eV).[8,9] Iwahara *et al.* were the first to demonstrate the potential of perovskite-type solid oxide proton conductors in energy-related applications in the early 1980s and 1990s.[10-15] Since then, the most intensively studied solid oxide proton conductors became doped barium cerate- and zirconate-based perovskite-type oxides, due to their high proton conductivities. The properties of $Ba(Ce,Zr)O_3$ perovskite proton conductors are well established and have been extensively reviewed.[8,9,15-22]

The crystal structure of $BaCeO_3$ and $BaZrO_3$ materials is based on the perovskite ABO_3 structure, which is composed by a network of corner-sharing BO_6 octahedra in which the larger A cations occupy the interstitial voids (Fig. 1a). Depending on the composition and the level of hydration, the ideal cubic perovskite structure (space group $Pm\bar{3}m$) is usually stable at high temperatures, with rhombohedral, orthorhombic, and monoclinic distortions at lower temperatures due to tilting of the octahedral units.[23-26] Proton conduction in these systems is enabled by the introduction of protonic defects *via* the dissociative absorption of water according to the hydration reaction,
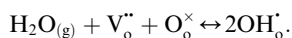
Fig. 1 (a) Cubic perovskite structure of $BaMO_3$ (M = Ce, Zr). (b) Schematic of a typical proton location along the O–O octahedron edge; the dotted line represents a hydrogen bond. (c) Representation of the proton conduction mechanism showing the reorientational rotation step (1), followed by proton hopping towards an adjacent oxygen atom (2).

$$H_2O_{(g)} + V_o^{\bullet\bullet} + O_o^{\times} \leftrightarrow 2OH_o^{\bullet}.$$

Water dissociates into a proton and a hydroxide ion by filling of an oxygen vacancy.[8,27] Pure $BaCeO_3$ and $BaZrO_3$ show limited proton incorporation due to the absence of available oxygen vacancies. Water absorption, and hence the creation of protonic species, is promoted by the introduction of oxygen vacancies *via* trivalent acceptor doping on the Ce/Zr-site. Y is the most commonly used acceptor dopant for effective proton conduction,[16,20] although numerous dopants have been tested.[28–32] The highest ionic conductivities are reported for barium cerate–zirconate solid solutions co-doped with Y and Yb.[33,34] The dissociative absorption of water results in the incorporation of a hydroxyl ion and in the formation of a covalent bond between a proton and a lattice oxygen atom. Protons are generally located in proximity of the O–O octahedron edge (Fig. 1b)[24,25,35,36] and have the tendency of forming hydrogen bonds with neighbouring oxygen atoms.[37] Proton transport follows a Grotthuss mechanism characterised by the fast rotational diffusion of the protonic defect around an oxygen atom (with activation energy of ~0.08–0.2 eV), followed by intra-octahedral hopping of a single proton towards a neighbouring oxide ion (~0.4–0.5 eV) and successive migration to an oxygen of an adjacent octahedron (Fig. 1c).[38–42] Under humid reducing atmospheres these systems show pure proton conduction, with a proton transport number t_H (which is the ratio of proton conductivity to total conductivity) close to unity.[13,43–45] However, at high temperatures and under higher partial pressure of oxygen, both barium cerates and zirconate present mixed oxide ion and electronic p-type conductivity, with t_H generally reducing to ~0.6–0.7 at 500 °C, due to an increase in the mobility of the oxygen vacancies and of the concentration of hole defects.[43,46,47]

Cerate and zirconate perovskites represent one of the most promising group of solid oxide proton conductors, as demonstrated by reports of excellent performances at low temperatures (300–600 °C) in proton ceramic fuel cells (PCFCs), electrolysis cells (PCECs), and reactor cells.[33,34,48–54] For example,

a peak power density of 548 mW cm^{-2} at 500 °C has been reported for a PCFC with an optimized $BaZr_{0.4}Ce_{0.4}Y_{0.1}Yb_{0.1}O_3$ electrolyte,[34] a value that greatly exceeds the performance of commercially available solid oxide fuel cells with yttria stabilized zirconia electrolytes.[5,48] However, barium cerate- and zirconate-based electrolytes also have some distinct disadvantages. $BaCeO_3$-based compounds are chemically unstable under CO_2 and H_2O, usually decomposing into $BaCO_3$ or $Ba(OH)_2$ and the corresponding oxide.[55–57] $BaZrO_3$-based materials show greater stability,[58,59] but their refractory nature makes grain growth difficult and results in a large grain boundary resistance which is detrimental for the overall conductivity.[16,20,60,61]

In the last two decades, research into alternative solid proton conductors possessing good ionic conductivity and stability has led to the discovery of proton conduction in several structural families. These include perovskite derivative oxides, systems containing tetrahedral moieties and fluorite-related oxides, with recent reports of materials exhibiting proton conductivities comparable to benchmark Y-doped $BaCeO_3$ and $BaZrO_3$ perovskite conductors (Fig. 2). These systems have promising properties, and in some cases show structural and proton conducting characteristics which are considerably different from the ones of conventional perovskite proton conductors (Table 1). Although citing numerous and state-of-the-art studies, it is beyond the scope of this perspective to give an exhaustive summary of all the properties of these alternative proton conducting oxide systems. Rather, this perspective
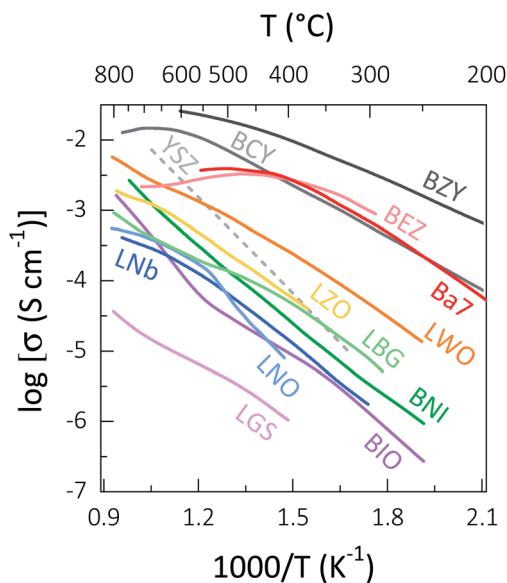

Fig. 2 Conductivities of selected solid oxide proton conductors: $Ba_7Nb_4MoO_{20}$ (Ba7, bulk);[68] $Ba_5Er_2Al_2ZrO_{13}$ (BEZ, total);[72] $BaNd_{0.8}$-$Ca_{0.2}InO_{3.90}$ (BNI, bulk);[106] $Ba_2In_2O_5$ (BIO, total);[114] $La_{0.99}Ca_{0.01}NbO_{4-\delta}$ (LNO, total);[138] $La_{0.8}Ba_{1.2}GaO_{3.9}$ (LBG, total);[167] $La_3Ga_{5.06}Si_{0.94}O_{14-\delta}$ (LGS, bulk);[179] $La_{1.95}Ca_{0.05}Zr_2O_{7-\delta}$ (LZO, total);[216] $La_{2.85}Sr_{0.15}NbO_{7-\delta}$ (LNb, total);[231] $La_{27}W_5O_{55.5}$ or "La_6WO_{12}" (LWO, total).[248] The bulk conductivity of $BaCe_{0.9}Y_{0.1}O_{3-\delta}$ (BCY),[8] the extrapolated bulk conductivity data of $BaZr_{0.8}Y_{0.2}O_{3-\delta}$ (BZY)[8] and the conductivity of the solid oxide ion electrolyte $Zr_{0.92}Y_{0.08}O_{1.96}$ (YSZ)[4] are shown for comparison.

Table 1 Summary of key properties of selected proton conducting oxide structures. Conductivity values are for measurements taken under typical conditions, *i.e.* air saturated with water (water partial pressure $pH_2O \sim 0.023$ atm). Where not reported, proton transference numbers were estimated from the values of conductivity in dry and humidified atmospheres, calculated according to the relationship $(\sigma_{wet} - \sigma_{dry})/\sigma_{wet}$ (see ref. 114). The obtained values are indicated with an asterisk and represent an overestimate, as they are calculated under the assumption that any electronic conductivity is negligible. The concentration of water uptake (which is directly correlated to the proton concentration, [OH]) observed under typical conditions at *ca.* room temperature is expressed as the number of water molecules per formula unit, nH_2O. When reported, the theoretical maximum number of water molecules that can be incorporated by the structure is also presented between brackets; this usually corresponds with the available vacant oxygen sites for water incorporation. Hydration enthalpy values (ΔH°_{hydr}) and experimental activation energy values of proton conductivity (E_a^H) are also reported

Compound	σ, 300 °C (S cm^{-1})	σ, 500 °C (S cm^{-1})	t_H, 300 °C	t_H, 500 °C	nH_2O	ΔH°_{hydr} (kJ mol^{-1})	E_a^H (eV)	Ref.
$BaCe_{0.9}Y_{0.1}O_{3-\delta}$	5.8×10^{-4}	7.1×10^{-3}	~1	0.8–0.9	~0.09 (0.1)	−163	0.53	8 and 46
$BaZr_{0.8}Y_{0.2}O_{3-\delta}$	3.5×10^{-3}	1.8×10^{-2}	~1	0.98	0.178 (0.2)	−22 ($T < 500$ °C) −93 ($T > 500$ °C)	0.47	8, 47 and 60
$Ba_7Nb_4MoO_{20}$	7.0×10^{-4}	4.0×10^{-3}	0.35	~0.80	~0.80 (1)	−18 ($T < 300$ °C) −76 ($T > 300$ °C)	0.57	68 and 69
$Ba_5Er_2Al_2ZrO_{13}$	9.8×10^{-4}	3.0×10^{-3}	~1	~1	~0.27 (2)	−13 ($T < 400$ °C) −192 ($T > 400$ °C)	0.40	72
$Ba_4Nb_2O_9$	—	6.0×10^{-6}	~0.2 (at 700 °C)		0.333 (0.333)	—	—	73
$Ba_4Ta_2O_9$	—	7.8×10^{-7}	~0.15 (at 700 °C)		~0.375 (1)	—	—	74
$BaLaInO_4$	4.0×10^{-8}	9.5×10^{-7}	~0.9	~0.6	0.62	—	0.87	82 and 83
$BaLa_{0.9}A_{0.1}InO_{3.95}$; A = Ca, Sr, Ba	0.6–1.8×10^{-6}	3.1–5.1×10^{-5}	~0.95	0.65–0.75	0.70–1.05	—	~0.80	73, 82 and 83
$La_2NiO_{4+\delta}$	4.0×10^1	3.6×10^1	—	—	0.03	—	—	89
$Pr_2NiO_{4+\delta}$	1.0×10^2	1.0×10^2	—	—	~0.03	—	—	89 and 90
$BaNd_{0.8}Ca_{0.2}InO_{3.90}$	3.3×10^{-6}	1.3×10^{-4}	0.47	0.53	0.011	—	0.67	106
$BaNd_{0.8}Ca_{0.2}ScO_{3.90}$	8.3×10^{-5} (at 600 °C)		0.62 (at 700 °C)		0.316	—	0.23–0.37	107
$Ba_2In_2O_5$	1.3×10^{-6}	3.2×10^{-5}	0.84	0.35	1 (1)	−74 to −63	~0.60	114–117 and 124
$RE_{0.99}Ca_{0.01}NbO_{4-\delta}$; RE = La, Nd, Tb, Er	—	2.4–6.3×10^{-5}	—	~1	—	−165 to −115	0.52–0.59	138
$RE_{0.99}Ca_{0.01}TaO_{4-\delta}$; RE = La, Nd, Gd, Er	—	2.8–4.7×10^{-5}	—	~1	—	−170 to −100	0.52–0.67	140
$La_{0.8}Ba_{1.2}GaO_{3.9}$	7.4×10^{-6}	1.4×10^{-4}	~0.90*	~0.80*	~0.08 (0.1)	—	0.44–0.75	167, 169 and 172
$La_3Ga_{5.06}M_{0.94}O_{14-\delta}$, M = Si, Ti, Sn	—	1.8–7.3×10^{-6}	—	~0.93*	—	−120 to −97	0.63–0.83	179
$La_3Ga_{5.6}Ta_{0.4}O_{14}$	—	3.0×10^{-6}	—	~0.92*	—	−85	0.72	180
$La_2Zr_2O_7$	5.0×10^{-7} (at 600 °C)		—	—	~0	—	—	200 and 201
$La_{1.95}Ca_{0.05}Zr_2O_{7-\delta}$	—	2.4×10^{-4}	—	~1	~0.03	−190	0.68	216–219
$Sm_{1.92}Ca_{0.08}Ti_2O_{7-\delta}$	1.6×10^{-5}	5.0×10^{-4}	~0.77*	—	~0.04 (0.08)	—	0.52–0.59	202

Table 1 (Contd.)

Compound	σ, 300 °C (S cm^{-1})	σ, 500 °C (S cm^{-1})	t_H, 300 °C	t_H, 500 °C	$n\mathrm{H_2O}$	$\Delta H^\circ_{\mathrm{hydr}}$ (kJ mol^{-1})	E_a^H (eV)	Ref.
$\mathrm{Sm_{1.92}Ca_{0.08}Sn_2O_{7-\delta}}$	2.7×10^{-6}	5.8×10^{-5}	~0.98*	—	~0.05 (0.08)	−100	0.83	203 and 204
$\mathrm{La_2Ce_2O_7}$	2.1×10^{-6}	2.4×10^{-4}	~1	~0.20	~0.20 (1)	−90 to −77	0.44–0.84	205–207
$\mathrm{La_{1.95}Ca_{0.05}Ce_2O_{7-\delta}}$	—	1.0×10^{-3}	—	~0.70*	—	—	—	222
$\mathrm{Nd_2Ce_2O_7}$	1.6×10^{-7}	2.7×10^{-5}	~0.40*	—	~0.03	−72	—	207
$\mathrm{La_3NbO_7}$	—	4.3×10^{-9}	—	~0.18*	2.5×10^{-3} (1)	—	—	233
$\mathrm{La_{2.97}Ca_{0.03}NbO_7}$	5.4×10^{-7}	2.0×10^{-5}	~0.54*	~0.40*	—	−117	0.77	231
$\mathrm{La_{2.85}Sr_{0.15}NbO_7}$	1.7×10^{-6}	6.6×10^{-5}	~0.50*	~0.42*	—	−116	0.77	231
$\mathrm{La_{2.60}Sr_{0.40}NbO_7}$	1.2×10^{-3} (at 600 °C)		~0.40 (at 600 °C)		—	—	—	230
$\mathrm{La_3TaO_7}$	—	1.3×10^{-7}	—	—	—	—	1.44	232
$\mathrm{La_{2.97}Ca_{0.03}TaO_7}$	1.7×10^{-7}	5.4×10^{-6}	~0.49*	~0.35*	—	−122	0.74	231
$\mathrm{La_{2.85}Ca_{0.15}TaO_7}$	4.7×10^{-7}	2.4×10^{-5}	~0.42*	~0.57*	—	−133	0.71	231
$\mathrm{La_{27}W_5O_{55.5}}$ ($\mathrm{La_6WO_{12}}$)	1.0×10^{-4}	1.0×10^{-3}	~1	~1	~0.40 (0.5)	−90 to −87	0.65	242, 244 and 247

provides an overview of the most relevant alternative and less established proton conducting materials, with a concise and up-to-date account of the structure–property relationships and the mechanistic aspects of hydration and ionic conduction. The aims are to highlight crucial and diverse structural features enabling proton incorporation and transport, and to invite further fundamental research into the proton conducting properties of other promising and unexplored oxide systems for the discovery of novel solid proton conductors.

2. Perovskite derivatives

The intrinsic flexibility and versatility of the perovskite structure allows the formation of a large number of derivatives via the introduction of defects and structural disorder. In addition, layered or intergrowth derivatives can be formed when the $\mathrm{ABO_3}$ layers are separated by different structural motifs. Some of these derivative systems are able to incorporate and enable fast diffusion of protonic defects thanks to the presence of intrinsic structural oxygen vacancies and flexible metal frameworks.

2.1 Hexagonal perovskites

Hexagonal perovskites form from mixed stacking sequences of hexagonal (h) and cubic (c) close-packing of $[\mathrm{AO_3}]$ layers, which result in the formation of face-sharing and corner-sharing $\mathrm{BO_6}$ octahedra.[62] Mixed combinations of corner-sharing and face-sharing octahedra can give rise to a variety of hexagonal

perovskite derivatives.[63] Different hexagonal polytypic structures are usually designated by specifying the total number of layers contained in the unit cell followed by a letter denoting the lattice type (H for hexagonal, C for cubic and R for rhombohedral).[64] These hexagonal structures are highly versatile and able to accommodate intrinsic cationic and anionic vacancies, with the formation of mixed metal coordination environments and different stacking arrangements.[63,65–67]

High proton conductivity in a hexagonal perovskite was first discovered in the cation deficient 7H derivative $\mathrm{Ba_7Nb_4MoO_{20}}$ by Fop et al.[68] In dry conditions, the conductivity of $\mathrm{Ba_7Nb_4MoO_{20}}$ is purely oxide ionic, with an oxide ion transport number of >0.99. Proton conduction is enabled under a humidified atmosphere, with a proton transport number of ~0.8 at 500 °C. The proton conductivity is 4.0×10^{-3} S cm^{-1} at 500 °C, comparable to doped barium cerate and zirconate perovskites. This system also presents good stability in reducing and $\mathrm{CO_2}$-rich environments and chemical compatibility with typical electrode materials such as NiO and $\mathrm{Ba_{0.5}Sr_{0.5}Co_{0.8}Fe_{0.2}O_{3-\delta}}$ (BSCF).[68]

In dry $\mathrm{Ba_7Nb_4MoO_{20}}$ the cation vacancies are ordered, and the average structure is composed by an intergrowth of 12R hexagonal perovskite units and oxygen deficient ($[\mathrm{BaO_2}]$) palmierite-like layers formed by $\mathrm{MO_x}$ polyhedra with mixed local 4-, 5-, and 6-fold coordination due to partial occupation of two different average crystallographic tetrahedral and octahedral oxygen sites ($\mathrm{O_{tet}}$ and $\mathrm{O_{oct}}$) (Fig. 3a).[69] Water is absorbed on the intrinsic oxygen vacancies present on the

This journal is © The Royal Society of Chemistry 2021
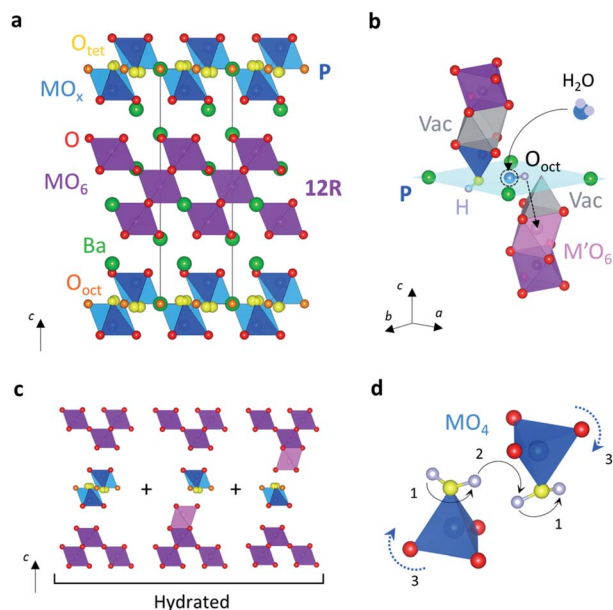
J. Mater. Chem. A, 2021, 9, 18836–18856 | 18839

Fig. 3 (a) Average structure of dry $Ba_7Nb_4MoO_{20}$ composed by an ordered intergrowth of palmierite-like layers (P) and 12R perovskite blocks. Blue and light blue polyhedra represents the average MO_4 and MO_6 polyhedra created by partial occupation of the two average oxygen crystallographic positions. (b) Representation of the water absorption on a vacant O_{oct} site. Hydration forces the shift of a metal from a palmierite site to an adjacent vacant octahedral metal site (Vac), with consequent formation of a $M'O_6$ unit. (c) Disordered local metal-vacancy stacking configurations composing the average structure of hydrated $Ba_7Nb_4MoO_{20}$. (d) Schematic of the ionic migration *via* rotation (1) and hopping (2) along the delocalised proton positions. Proton transport is assisted by rotational motion of the flexible MO_x units (3).

Fig. 4 (a) Crystal structure of $Ba_5Er_2Al_2ZrO_{13}$ composed by the stacking of cubic $[BaO_3]$ and oxygen deficient hexagonal $[BaO]$ layers. (b) Representation of the absorption of a molecule of water on the intrinsic oxygen vacancy on the hexagonal $[BaO]$ layer. Protons are bound to the shared apical oxygen atoms of the Al_2O_7 unit.

palmierite-like layer and predominantly distributed on the average O_{oct} sites.[68,69] The water absorption leads to disordering of the metal-stacking vacancy distribution due to a shift of the cation in the palmierite layer towards an adjacent mutually
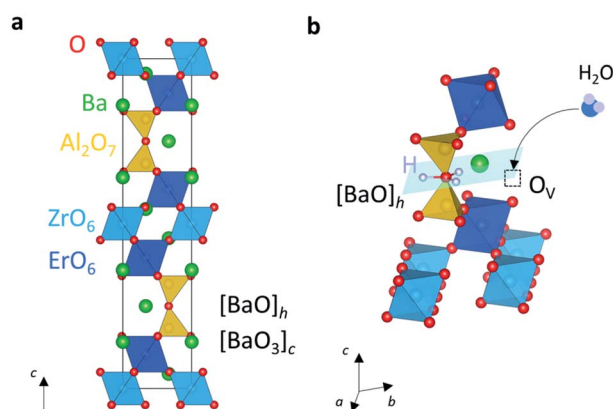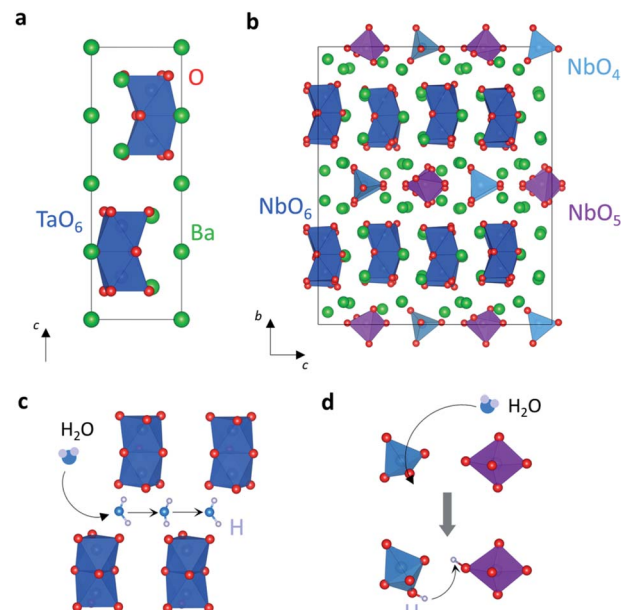

Fig. 5 (a) Structure of $6H–Ba_4Ta_2O_9$. (b) Crystal structure of the γ-phase of $Ba_4Nb_2O_9$ in which Nb has mixed 4-, 5-, and 6-fold coordination. (c) Representation of the water intercalation and migration in the structural void between the Ta_2O_9 dimers present in the structure of $6H–Ba_4Ta_2O_9$. (d) Hydration of γ-$Ba_4Nb_2O_9$ *via* formation of NbO_4OH_4 units and proton hopping between adjacent isolated polyhedra.

exclusive vacant site, as result of the repulsion between a proton pointing towards the nearest MO_x unit and a metal cation (Fig. 3b). Partial occupation of the two metal sites results in the formation of disordered local stacking configurations creating a complex average network of isolated, face-sharing and corner-sharing polyhedral units in the hydrated material (Fig. 3c).

The significant structural flexibility of $Ba_7Nb_4MoO_{20}$ allows the accommodation of the local cation and anion disorder introduced by hydration and enables a high concentration of water uptake, ≥ 0.8 molecules of H_2O per formula unit.[68,69]

Neutron diffraction experiments and atomistic calculations demonstrate that protons are in proximity of the average O_{tet} and O_{oct} sites.[69] The positional oxide ion disorder generated by the close proximity of available oxygen sites due to the particular topology of the palmierite-like layers leads to delocalisation of the protonic defects over a variety of low energy configurations around their equilibrium site. Such delocalisation results in the creation of two-dimensional low energy transport pathways along the palmierite-like layers, where the proton defects can migrate *via* rotation and hopping motion with calculated migration energies in the range 0.18–0.61 eV depending on the local configuration (Fig. 3d). Importantly, the proton diffusion is assisted by the high flexibility and rotational mobility of the isolated variable coordination MO_x units. Proton diffusion is usually slower in lower symmetry perovskite oxides such as orthorhombic $SrCeO_3$ and $CaZrO_3$, due to an additional enthalpy contribution needed for tilting of adjacent octahedra closer enough to allow proton hopping.[8,70] Localisation of the

18840 | *J. Mater. Chem. A*, 2021, **9**, 18836–18856

This journal is © The Royal Society of Chemistry 2021

protonic defects also generally leads to reduced proton conductivity, as in the case of the hexagonal 6H phase of Sc-doped $BaTiO_{3-\delta}$.[71] In hydrated $Ba_7Nb_4MoO_{20}$, frustration of the proton sub-lattice and the high dynamic flexibility of the variable coordination MO_x moieties enable fast proton transport.

Another member of the hexagonal perovskite family displaying high proton conductivity is $Ba_5Er_2Al_2ZrO_{13}$.[72] This system is a 10H hexagonal perovskite derivative with a structure composed by the stacking of cubic $[BaO_3]$ and oxygen deficient hexagonal $[BaO]$ layers. The intrinsic oxygen deficient layers result in the creation of tetrahedral sites which are occupied by the aluminium atoms to form Al_2O_7 units (Fig. 4a).

While in dry air the conductivity is electronic p-type, $Ba_5Er_2Al_2ZrO_{13}$ presents a large protonic component in humidified air, showing a proton transport number of ∼1 from 300 to 600 °C and conductivity of 3.0×10^{-3} S cm^{-1} at 500 °C.[72] Water is absorbed on the intrinsic oxygen vacancies of the hexagonal $[BaO]$ layer, with the proton sites located on the apical oxygen atoms of the Al_2O_7 units (Fig. 4b).[72] Both $Ba_7Nb_4MoO_{20}$ and $Ba_5Er_2Al_2ZrO_{13}$ share the existence of oxygen deficient Ba–O layers with intrinsic oxygen vacancies enabling water absorption and fast proton transport.

Compounds of the series $Ba_4M_2O_9$ (M = Nb, Sb, Ta) are hexagonal derivatives exhibiting mixed oxide ion, proton and electronic conduction.[73–75] While the ionic conductivities are far below those of representative proton conductors (<10^{-5} S cm^{-1} at 400 °C), these systems present complex polymorphic behaviour and interesting hydration and conduction mechanisms. The Nb and Ta compounds have the same low temperature α polymorph, which is composed by partially disordered isolated face-sharing octahedral $(Nb/Ta)_2O_9$ dimers separated by large voids. The high temperature phases of $Ba_4Ta_2O_9$ and $Ba_4Sb_2O_9$ both exhibit a 6H structure formed by face sharing octahedral units connected to BaO_6 octahedra through corner-sharing (Fig. 5a).[74,76] On the other hand, the niobate presents a high temperature orthorhombic γ-phase composed by layers of isolated face-sharing Nb_2O_9 dimers separated by ordered rows of isolated NbO_4 and NbO_5 units (Fig. 5b).[77]

The high temperature 6H–$Ba_4Ta_2O_9$ and γ-$Ba_4Nb_2O_9$ phases can be quenched to room temperature and are able to incorporate a substantial amount of water. In 6H–$Ba_4Ta_2O_9$, discrete water molecules are intercalated in the void between the Ta_2O_9 dimers. *Ab initio* molecular dynamics (AIMD) simulations show that the H_2O molecule unusually does not dissociate into H^+ and OH^-, migrating intact through the voids (Fig. 5c).[78] In the γ-$Ba_4Nb_2O_9$ phase, water is absorbed *via* hydroxylation of the NbO_4 tetrahedra and hydrogenation of the NbO_5 trigonal bipyramids to give two NbO_4OH_4 units. AIMD simulations evidence that proton conduction mainly occurs within the *ab* plane of the NbO_5 polyhedra by hopping between oxygen atoms of adjacent NbO_4OH units (Fig. 5d).[78]

Other hexagonal perovskite derivatives which exhibit proton conductivity are cation deficient 12R $Sr_3RENb_3O_{12}$ (RE = La, Nd) and 5H $Ba_5Nb_4O_{15}$.[79–81] The structures of both compounds are composed by trimers (12R) or tetramers (5H) of corner-sharing NbO_6 octahedra spaced by cationic vacancies. These systems present mixed ionic and electronic conduction, with proton transport dominating under wet oxidising conditions. The ionic conductivities are modest (∼10^{-6} S cm^{-1} at 550 °C), but their values can be substantially increased by acceptor doping on the Nb-site.[79,80]

These accounts highlight the inherent structural versatility of hexagonal perovskite derivatives of accommodating cation and anion defects/disorder and their ability in incorporating and enabling transport of protonic defects through different mechanisms. Even though reports of proton conduction in these systems are quite scarce, the most recent results on $Ba_7Nb_4MoO_{20}$ and $Ba_5Er_2Al_2ZrO_{13}$ are particularly promising and encourage further exploration of proton conduction in the vast family of hexagonal perovskite derivatives.

2.2 Ruddlesden–Popper structures

Layered perovskite derivatives form when perovskite-like slabs are spaced by some different structural motif. Ruddlesden–Popper (RP) phases are a particular class of layered perovskites with general formula $A_{n+1}B_nO_{3n+1}$. The structures of RP phases are composed by *n* perovskite layers alternated with rock-salt slabs, thus forming a framework in which *n* layers of corner-sharing BO_6 octahedra are separated by AO layers (Fig. 6a). $BaLaInO_4$-based oxides have K_2NiF_4-type structures (*n* = 1) and exhibit mixed oxide ion and proton conduction.[82–85] These
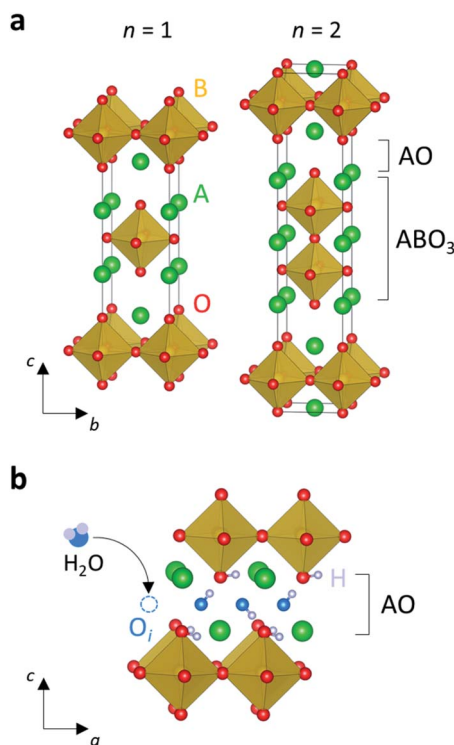

Fig. 6 (a) $A_{n+1}B_nO_{3n+1}$ Ruddlesden–Popper structures, A_2BO_4 (*n* = 1) and $A_3B_2O_7$ (*n* = 2). (b) Schematic of the absorption of a water molecule on the interstitial oxygen site (O_i) along the rock-salt AO layer. Protons are located at the interstitial oxygen position forming an OH and on the apical oxygen of the metal octahedra.
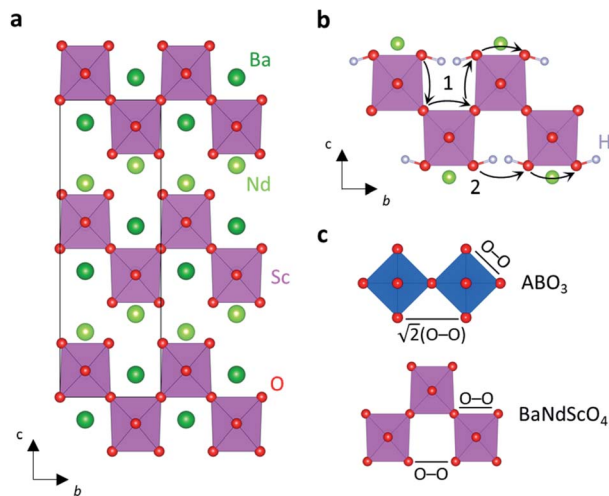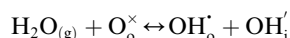
This journal is © The Royal Society of Chemistry 2021

J. Mater. Chem. A, 2021, **9**, 18836–18856 | **18841**

Fig. 7 (a) Structure of BaNdScO$_4$. (b) Proton locations and representation of the intra-octahedral (1) and inter-octahedral (2) proton diffusion pathways. Ba atoms are omitted for clarity. (c) Schematic of the intra- and inter-octahedral O−O distances in cubic ABO$_3$ perovskites and BaNdScO$_4$. In the cubic ABO$_3$ perovskite structure the inter-octahedral distance is approximately $\sqrt{2}$ times the O−O intra-octahedral separation. In contrast, the intra- and inter-octahedral distances are similar in BaNdScO$_4$.

Fig. 8 (a) Brownmillerite A$_2$B$_2$O$_5$ structure composed by alternating layers of BO$_6$ octahedra (B$_{oct}$) and BO$_4$ tetrahedra (B$_{tet}$). (b) Representation of the transition from dry orthorhombic Ba$_2$In$_2$O$_5$ to the fully hydrated tetragonal phase BaInO$_3$H. Water is absorbed onto the intrinsic oxygen vacancies (O$_V$) distributed along the tetrahedral layer. Protons in the tetragonal BaInO$_3$H structure occupy two distinct average positions: H1, which is partially occupied, and H2. (c) Local protons configuration.

systems have generally large protonic components with proton transport numbers >0.80 under wet conditions at temperatures below 450 °C, although their conductivities are rather low (10^{-6} to 10^{-5} S cm^{-1}). Several ferrite and nickelate RP oxides with general compositions A$_2$BO$_4$ ($n = 1$) or A$_3$B$_2$O$_7$ ($n = 2$) (A = Sr, La, Nd, Pr; B = Fe, Ni) show triple mixed conductivity (i.e. protonic, oxide ion and electronic). These systems present good chemical compatibility with barium cerate and zirconate conductors[86–88] and are currently investigated for application as electrodes in hydrogen-based electrochemical devices.[89–97] For example, measurements on symmetrical cells based on a Y-doped BaCeO$_3$ electrolyte with Pr$_2$NiO$_{4+\delta}$ and La$_2$NiO$_{4+\delta}$ cathodes demonstrated high oxygen reduction reaction (ORR) activity and area specific resistance (ASR) similar to BSCF ($\leq$1 Ω cm^2 at 600 °C).[89,90,98] High power outputs (1070 mW cm^{-2} at 700 °C) have also been reported for a PCFC with a BaZr$_{0.1}$Ce$_{0.7}$Y$_{0.1}$-Yb$_{0.1}$O$_{3-\delta}$ electrolyte and the RP $n = 2$ cathode material Pr$_2$-BaNiMnO$_{7-\delta}$, with no degradation at 0.7 V at 600 °C for 100 h.[99]

RP structures are notoriously able to accommodate excess interstitial oxygen.[100] In contrast with acceptor doped perovskites, the dissociative absorption of water in these RP systems occurs via hydration of the available interstitial oxygen sites along the rock-salt layers,[90,93,101,102] following the relationship:

$$H_2O_{(g)} + O_o^\times \leftrightarrow OH_o^\bullet + OH_i'$$

OH occupies an interstitial site, while a hydrogen atom is bonded to an apical oxygen of the metal octahedra (Fig. 6b). Preliminary calculations (without the consideration of the interstitial oxygen defects) on La$_2$NiO$_4$/La$_3$Ni$_2$O$_7$ have evidenced two possible proton migration pathways, inter-layers, i.e. across two adjacent AO layers, and inner-layer.[102] The inter-layers
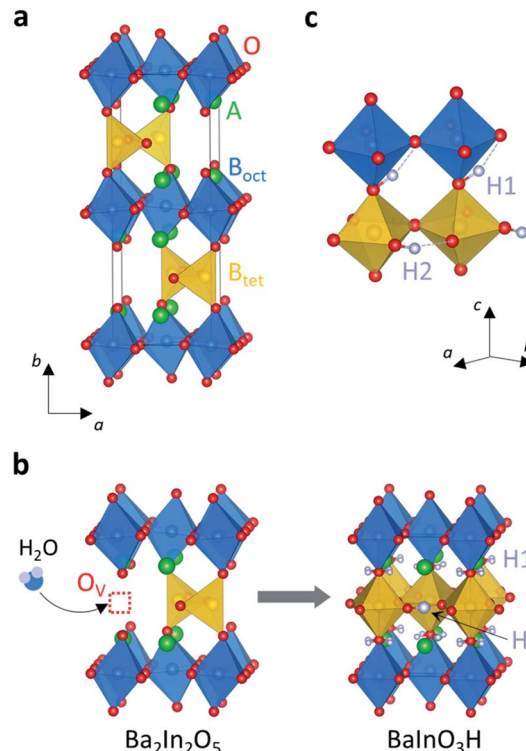
pathway has a very large energy barrier (>3.5 eV) and probably does not contribute to the proton diffusion. The inner-layer pathway presents considerably lower energy barrier (1.29–1.66 eV) and involves a Grotthuss mechanism with rotation and hopping of the protons between the apical and equatorial oxygen positions of the metal octahedra (similarly to the case of cubic perovskites).[102,103]

Compounds of the series BaNdMO$_4$ (M = In, Sc) are RP derivatives.[104,105] Their structures are composed by (Ba$_{3/4}$Nd$_{1/4}$MO$_3$)$_2$ perovskite layers alternated with NdO rock-salt blocks. They differentiate from the common RP structure because the edge of the MO$_6$ octahedron faces the rock-salt unit (Fig. 7a). These systems are mixed oxide ionic and electronic conductors and recent reports have revealed significant proton conductivity in acceptor-doped materials of composition BaNd$_{1-x}$Ca$_x$MO$_{4-x/2}$.[106,107] The doped indate exhibits higher conductivity than the Sc compound. At 500 °C, BaNd$_{0.8}$Ca$_{0.2}$InO$_{3.90}$ exhibits conductivity of 1.3×10^{-4} S cm^{-1} under humidified air and a proton transport number of $\sim$0.53, although this system presents poor chemical stability in a humid atmosphere.[106]

Water is absorbed onto the oxygen deficient layer at the interface between the perovskite and the rock-salt layers, with the protons located on the equatorial oxygen atoms of the MO$_6$ octahedra.[107] Protons diffuse via rotational and hopping

motions along the lowest energy intra- and inter-octahedral pathways, which have similar migration barriers of 0.63 eV and 0.69 eV respectively (Fig. 7b). Inter-octahedral proton hopping is generally unfavoured in cubic perovskite structures due to the large inter-octahedral O–O distance (Fig. 7c). Inter-octahedral diffusion predominantly occurs in lower symmetry perovskite-type structures, where the hopping distance is shortened by octahedral tilting.[8,70] However, in the BaNdMO$_4$ structure the inter-octahedral O–O separation is comparable to the intra-octahedral O–O distance, thus enabling both pathways (Fig. 7c).[107]

The results on RP materials suggest that similar layered perovskite structures could potentially support analogous mechanisms of proton incorporation and transport. Dion-Jacobson phases with general formula MA$_{n-1}$B$_n$O$_{3n+1}$ (M = alkali metal) are closely related to the RP structure, having a layer of alkali metal as the separating motif between the perovskite blocks.[108] Aurivillius phases are constituted by perovskite layers spaced by rock-salt BiO sheets in which Bi is in a square-based pyramidal coordination.[109] Both these structure systems support oxide ion conduction,[108,109] with signatures of proton conductivity in some Dion–Jacobson materials,[110,111] and could therefore constitute an interesting avenue of research into novel layered perovskite proton conductors.

2.3 Brownmillerite materials

Another class of layered perovskite derivatives is the brownmillerite family. The brownmillerite structure, with general formula A$_2$B$_2$O$_5$, can be described as an oxygen deficient perovskite structure, having 1/6 of oxygen sites empty. The intrinsic oxygen vacancies are fully ordered in rows along the [110]$_p$ direction (where the subscript p denotes the perovskite subcell) and form corner-sharing octahedral perovskite layers alternated with tetrahedral layers (Fig. 8a). The most studied brownmillerite material is the oxide ion conductor Ba$_2$In$_2$O$_5$.[112] At high temperature (T > 900 °C), disordering of the oxygen vacancies leads to a transition to a highly conductive cubic phase.[112,113]

Under humidified atmosphere, Ba$_2$In$_2$O$_5$ exhibits significant proton conductivity, with a proton transport number >0.70 below 400 °C.[114,115] The large number of intrinsic oxygen vacancies enables the water absorption. Ba$_2$In$_2$O$_5$ can uptake a considerable concentration of water, forming the fully hydrated phase Ba$_2$In$_2$O$_5$(H$_2$O), or BaInO$_3$H.[116–118] Upon hydration, the dry brownmillerite structure transforms from orthorhombic to a tetragonal perovskite-like phase (at T < 300 °C), where the intrinsic oxygen vacancies in the tetrahedral layer are fully occupied by the water oxygen atoms (Fig. 8b).[118,119] Protons are located on two different sites; H1 is on a partially occupied position bonded to an apical octahedral oxygen, while H2 is on a fully occupied site lying between two equatorial oxygen atoms corresponding with the tetrahedral layer in the dehydrated structure.[120–122] Protons are ordered according to a defined local configuration, in which H1 is hydrogen bonded towards the equatorial oxygen of the octahedral layer of the dry structure (Fig. 8c).[123] The hydrogen bond configuration affects the

mobility of the protonic defects and restricts the number of sites available for hopping, thus resulting in anisotropic proton conduction.[122,124]

The conductivity of Ba$_2$In$_2$O$_5$ under humidified conditions is ~10^{-5} S cm^{-1} at 400 °C.[114] Doping on the In-site generally leads to stabilisation of the perovskite-like structure and to increased proton conductivity.[118,125] Interestingly, the cubic phase can be stabilised also by oxyanion doping via the introduction of silicate, phosphate or sulfate groups, with the conductivity increasing to 2.4 × 10^{-3} S cm^{-1} at 400 °C in Ba$_2$In$_{1.8}$Si$_{0.2}$O$_{5.1}$.[126,127] Ba$_2$In$_2$O$_5$ decomposes in hydrogen-containing atmospheres above 500 °C, with the formation of In metal and BaCO$_3$ and a considerable reduction of the ionic conductivity over time.[115] Due to the presence of electronic conductivity and the generally poor stability under reducing conditions, fuel cells with Ba$_2$In$_2$O$_5$-based electrolytes exhibit generally low power densities (<10 mW cm^{-2} at 600 °C).[128]

Other brownmillerite compounds exhibiting proton conductivity are Ba$_2$InGaO$_5$ and Sr$_2$ScGaO$_5$.[129,130] The ionic conductivity of Ba$_2$InGaO$_5$ is quite modest due to ordering of the In and Ga cations along the stacking axis, which further stabilises the orthorhombic brownmillerite structure.[129] Sr$_2$ScGaO$_5$ also exhibits a moderate protonic component.[130] However, heavily Zn-doped Sr$_2$ScGaO$_5$ (Sr$_2$Sc$_{1-x}$Zn$_x$GaO$_{5-0.5x}$, 0.4 ≤ x ≤ 0.6) presents a highly disordered and highly oxygen deficient perovskite structure with a peculiar one-coordinate oxygen site and shows significant proton conductivity, with three orders of magnitude increase in the conductivity in comparison with the parent compound.[130]
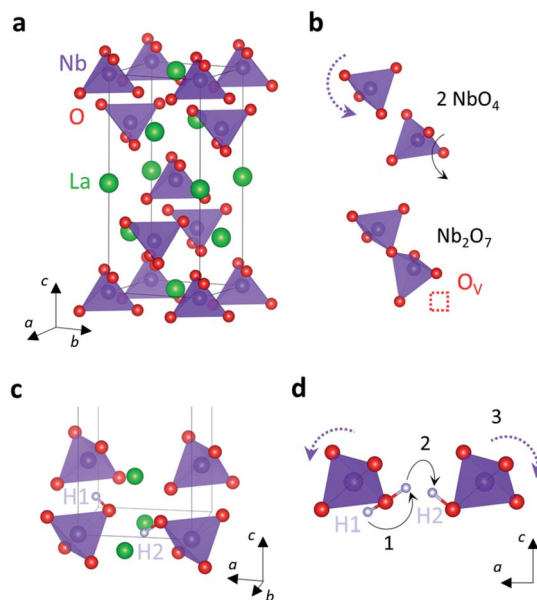

Fig. 9 (a) Tetragonal LaNbO$_4$ scheelite structure composed by isolated NbO$_4$ tetrahedra. (b) Schematic of the oxygen vacancy stabilisation. Two NbO$_4$ tetrahedral units relax and condensate to form a Nb$_2$O$_7$ unit in the neighbourhood of the vacant oxygen site (O$_V$). (c) Protons positions in scheelite LaNbO$_4$. (d) Representation of the long-range H1–H2 proton migration showing rotation (1) and hopping onto an adjacent tetrahedron (2), assisted by motion of the isolated tetrahedral units (3).

This journal is © The Royal Society of Chemistry 2021

J. Mater. Chem. A, 2021, 9, 18836–18856 | 18843

A recent study has demonstrated that the brownmillerite $Sr_2Co_2O_5$ can absorb one H per formula unit, forming hydronated $HSrCoO_{2.5}$ (although this phase is stable only up to 160 °C).[131,132] Atomistic calculations show that protons are distributed among apical and equatorial octahedral oxygen sites and that they adopt a wide range of configurations with similar energies.[133] The cooperative transition between the different configurations creates a frustrated proton sub-lattice enabling high proton mobility. Measurements on a thin film of $HSrCoO_{2.5}$ showed conductivity of 0.33 S cm^{-1} at 140 °C.[132] However, further measurements on a bulk dense sample are required to confirm such high conductivity and rule out any effects from proton transport along physisorbed water at the inner surface of the porous film.[134]

Brownmillerite-based materials with intrinsic oxygen vacancies offer potential of high proton conductivity, thanks to the ability of the structure of incorporating large concentrations of water. Other brownmillerite compounds showing oxygen intercalation ability may be able to incorporate water and enable proton transport,[135–137] thus constituting further candidate proton conductors.

3. Oxides with tetrahedral moieties

Proton conduction has been reported in various systems possessing tetrahedral moieties as their principal structural feature. These tetrahedral units are present in isolated or corner-sharing motifs and generally assist the protonic transport thanks to their high flexibility and rotational mobility.

3.1 REMO$_4$ phases

Haugsrud and Norby were the first to demonstrate high proton conductivity in REMO$_4$-based materials, namely in several acceptor doped ortho-niobates and ortho-tantalates with general formula $RE_{1-x}A_xMO_4$ (RE = La, Gd, Nd, Tb, Er, Y; A = Ca, Sr, Ba; M = Nb, Ta).[138] Compared to acceptor doped perovskite conductors, proton conductivity in these ortho-niobates and ortho-tantalates is attained for relatively low doping levels (x = 0.01–0.05). Proton conduction is dominant (proton transport number ~1.0) under humidified and reducing atmospheres below 800 °C, while the conductivity is p-type electronic under oxidizing conditions at high temperatures.[138–140]

These rare earth ortho-niobates and ortho-tantalates are isostructural, crystalising in the monoclinic fergusonite-type structure at low temperatures and in the tetragonal scheelite phase at high temperatures (Fig. 9a). Both structure types are composed by isolated tetrahedral units sharing corners with REO$_{12}$ dodecahedral units; the low temperature fergusonite structure can be considered as a slight monoclinic distortion of the tetragonal high temperature phase.[141] The transition temperature depends on the composition and for LaNbO$_4$ is in the range 500–530 °C.[139,142] The fergusonite–scheelite transition in LaNbO$_4$ has originally been described as a second order transition between the ferroelastic monoclinic phase and the paraelastic tetragonal phase.[143] However, recent reports suggest a reconstructive first order transition induced by displacement of the Nb cation from the centre of the tetrahedron and change in NbO coordination from 4 in the scheelite phase to a 6-coordinated distorted octahedral arrangement in the fergusonite phase, with two long and four short Nb–O distances.[144,145] The fergusonite–scheelite transition is relevant to the proton conductivity, since it coincides with a reduction in the activation energy for proton transport (from 0.78 eV to 0.55 eV in $La_{0.99}Ca_{0.01}NbO_{4-\delta}$), which is associated to an increase in the mobility of the proton defects in the scheelite phase.[138,142] However, the presence of this transition may be detrimental for practical electrolyte applications due to the different thermal expansion coefficients of the two phases (around 15×10^{-6} °C^{-1} for the low temperature monoclinic phase and 8.6×10^{-6} C^{-1} for the high temperature polymorph) and the tendency to microcracking.[146] The scheelite phase can be stabilised at room temperature *via* substitution of Nb with isovalent cations such as V, As, and Sb, generally resulting in an increase of the conductivity at lower temperatures.[147–150]

Acceptor doping of LaNbO$_4$ introduces extrinsic oxygen vacancies, enabling water absorption. Atomistic calculations on the scheelite LaNbO$_4$ structure have demonstrated that oxygen vacancies are stabilized by local relaxation and condensation of the NbO$_4$ tetrahedra around a vacant oxygen site to form Nb_2O_7 or Nb_3O_{11} polyhedral linkages (Fig. 9b).[151,152]

The thermodynamics of hydration and the proton mobility depend on the size of the rare-earth element. Hydration is more exothermic (*i.e.* more favourable) as the rare-earth cation becomes smaller, with the enthalpy of the water absorption reaction reducing from −115 kJ mol^{-1} in the La niobate, to −165 kJ mol^{-1} for the Er-containing composition.[138] This trend is in contrast with REPO$_4$ phosphates, of which crystal structures are composed by similar isolated tetrahedral units.[153] On the other hand, the proton mobility is lower when the RE cation is smaller due to lattice size effects and to the decreasing lattice polarizability of the smaller unit cell.[138] The LaNbO$_4$-based materials exhibit the highest conductivity, with a value of ~10^{-3} S cm^{-1} at 800 °C in $La_{0.99}Ca_{0.01}NbO_{4-\delta}$.[138,139]

Structural optimization calculations on scheelite LaNbO$_4$ have demonstrated that protons are located on two stable positions in proximity of the only crystallographic oxygen site: along the edge of the NbO$_4$ tetrahedron (H1, lowest energy) and on a site between two lanthanum ions (H2) (Fig. 9c).[152,154] Long-range proton migration occurs along the pathway connecting the H1 and H2 sites, through rapid rotation of the proton around the oxide ion (with an energy barrier of 0.04–0.06 eV) followed by hopping between two adjacent tetrahedra (with a barrier of 0.41 eV) (Fig. 9d).[154]

Despite exhibiting lower conductivities than perovskite cerate oxides, doped LaNbO$_4$-based materials shows greater stability in CO$_2$-containing atmospheres,[155] which together with a proton transport number close to unity make these materials highly interesting for fuel cell applications. Tests on different proton-conducting electrode materials have demonstrated generally good chemical compatibility of LaNbO$_4$ materials with LaMO$_3$ (M = Mn, Fe, Co) perovskite type cathodes and NiO,[155–157] while they show poor compatibility with proton-

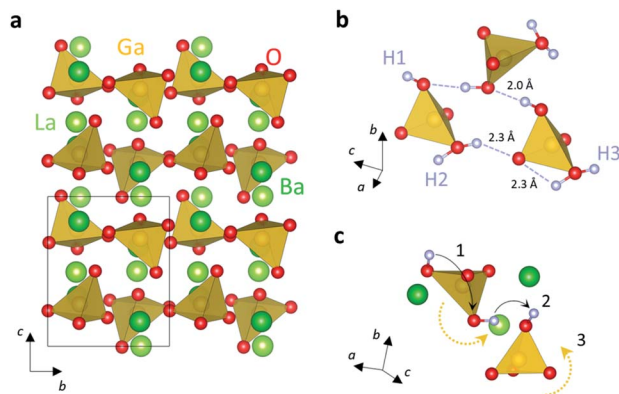**18844** | *J. Mater. Chem. A*, 2021, **9**, 18836–18856

This journal is © The Royal Society of Chemistry 2021

Fig. 10 (a) Crystal structure of $La_{1-x}Ba_{1+x}GaO_{4-x/2}$, which is composed by distorted isolated GaO_4 tetrahedra and alternated layers of Ba and La cations. (b) Locations of the three different stable proton sites and representation of the mixed inter- and intra-tetrahedral hydrogen bond interactions. The shorter inter-tetrahedral O···H distance is indicative of a stronger interaction. (c) Proton diffusion pathway composed by intra-tetrahedral exchange (1) followed by hopping onto an oxygen of adjacent tetrahedron (2). The inter-tetrahedral jump is assisted by rotation of the tetrahedral units (3).

conducting ceramic anodes because of undesirable reactions at high temperatures.[158] Anode supported fuel cell with $La_{0.99}$-$Ca_{0.01}NbO_{4-\delta}$ electrolytes have shown modest peak power densities (24 mW cm^{-2} at 750 °C) due to the large polarization resistance between the electrodes and the electrolyte (20–40 Ω cm^2 at 800 °C).[155,157,158]

Acceptor doped monazite-type systems $LaVO_4$, $LaAsO_4$, and $LaSbO_4$ also present significant proton conductivity under humidified atmosphere.[159–161] The monoclinic monazite structure is similar to the scheelite structure and is composed by isolated distorted MO_4 tetrahedra sharing their edges with LaO_9 polyhedra.[162] Doped $LaVO_4$ and $LaAsO_4$ exhibit the highest conductivities; the proton conductivity of $La_{0.99}Ca_{0.01}VO_{4-\delta}$ is $\sim 3 \times 10^{-4}$ S cm^{-1} at 800 °C, although the ortho-vanadate is unstable under reducing conditions.[159]

Atomistic calculations on $LaAsO_4$ have revealed that extrinsic oxygen vacancies are introduced via condensation of two adjacent tetrahedra to form a pyro-arsenate As_2O_7 unit, similar to the case of $LaNbO_4$.[160] Protons are statistically distributed on two lowest energy positions located on two non-equivalent oxygen sites within the same tetrahedron. Interestingly, while incorporated protons in oxides generally reside around oxide ions forming OH groups, in $LaAsO_4$ the protonic defects are stabilised as covalent hydrogen arsenate ions, $HAsO_4^{2-}$.[159] During the inter-tetrahedral proton migration, the host lattice mainly exhibits rotational and translational relaxation with little distortion of the AsO_4 polyhedra, a feature that is common in proton conducting oxides with isolated tetrahedral moieties and in contrast with ABO_3 perovskites where proton transport is generally accompanied by large distortion of the corner-sharing BO_6 octahedra.[163]

A variety of compositions crystallize with the scheelite, monazite or in closely related structures[162,164–166] and could offer an interesting crystal chemistry space for the investigation of
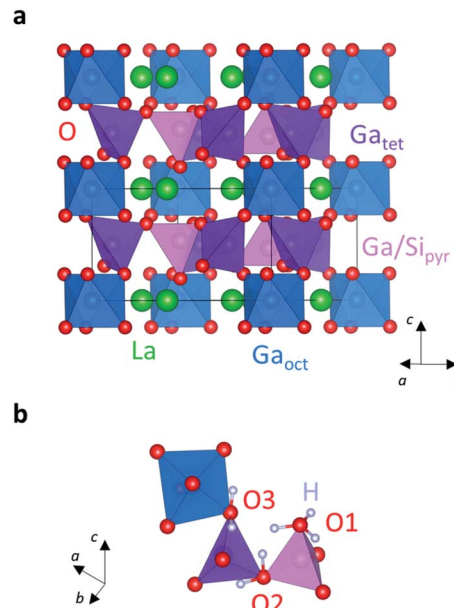
proton conduction in systems with isolated tetrahedral moieties.

3.2 Gallium-based oxides

High proton conductivity has been reported in lanthanum–barium gallates of general formula $La_{1-x}Ba_{1+x}GaO_{4-x/2}$.[167,168] The parent compound $LaBaGaO_4$ possesses an orthorhombic β-K_2SO_4-type structure composed by isolated distorted GaO_4 tetrahedra and ordered alternating layers of Ba and La atoms (Fig. 10a). $LaBaGaO_4$ shows high resistivity with limited proton conduction. Variation of the La/Ba ratio to produce the solid solution $La_{1-x}Ba_{1+x}GaO_{4-x/2}$ results in the introduction of oxygen vacancies enabling high ionic conduction. The member with $x = 0.2$, $La_{0.8}Ba_{1.2}GaO_{3.9}$, shows proton conductivity of $\sim 10^{-4}$ S cm^{-1} at 500 °C under humidified O_2.[167,168]

The oxygen vacancies in $La_{0.8}Ba_{1.2}GaO_{3.9}$ are accommodated through the condensation of two adjacent GaO_4 units to form a Ga_2O_7 group (in a way analogous to acceptor doped $LaNbO_4$).[169] On the local scale, the oxygen vacancies are pinned to the nearest-neighbour cation site by the Ba'_{La} defects and there is no ordering of the Ga_2O_7 units.[170] Water incorporation induces the break-up of the Ga_2O_7 units,[169] according to the reaction

$$Ga_2O_7 + H_2O \rightarrow 2GaO_4H.$$
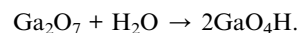
Protons in $La_{0.8}Ba_{1.2}GaO_{3.9}$ are located on three different sites, pointing almost perpendicular to the Ga–O bond direction (Fig. 10b).[171] Protons migrate following a curved path between

Fig. 11 (a) Crystal structure of langasite $La_3Ga_5SiO_{14}$ showing the alternating layers of GaO_6 octahedra and tetrahedral and planar trigonal pyramidal GaO_4 units. The pyramidal site is partially occupied by Ga and Si. (b) Calculated stable proton locations in $La_3Ga_5SiO_{14}$. The lowest energy proton positions are on the oxygen site shared by an octahedral and a tetrahedral unit, O3.

This journal is © The Royal Society of Chemistry 2021

J. Mater. Chem. A, 2021, **9**, 18836–18856 | **18845**

two intra-tetrahedral oxide ions due to the repulsive interactions with nearby large Ba/La cations, followed by jump onto an oxygen of an adjacent GaO_4 unit (Fig. 10c).[169]

The rate-determining step for proton diffusion is the intratetrahedra migration, which has a considerably higher energy barrier ($\sim$0.4–0.7 eV) than the inter-tetrahedral hopping ($\sim$0.07 eV).[169,172] The latter is favoured by the inter-tetrahedral hydrogen bond O···H interactions, which are shorter ($\sim$2.0 Å) than the intra-tetrahedral ones ($\sim$2.3 Å),[171,173] thus highlighting the significance of the H bonding configuration (Fig. 10b) in defining the mechanism of proton transport in $La_{0.8}Ba_{1.2}GaO_{3.9}$. Importantly, the inter-tetrahedral proton migration is also facilitated by the rotational mobility of the GaO_4 units,[174,175] a mechanism that is similar to the rapid phosphate group reorientation in the solid-acid protonic conductor CsH_2PO_4.[176] It is worth noticing that while intra-polyhedral hoppings are common in perovskite systems with corner-sharing octahedral units, intra-tetrahedral proton hopping is particularly unfavoured in $La_{0.8}Ba_{1.2}GaO_{3.9}$ and in other oxide structures with isolated tetrahedral units such as $LaNbO_4$ and $LaAsO_4$.[163,177]

Proton conductivity has been reported in gallium-based oxides having general composition $RE_3Ga_5MO_{14}$ (RE = La, Nd; M = Si, Ti, Sn, Ta).[178–180] These compounds belong to the langasite family and their structure is composed by alternated layers of Ga in a mixed 6-fold (octahedral) and 4-fold (tetrahedral/planar trigonal pyramidal) coordination, with the pyramidal site being partially occupied by the Ga/M cations (Fig. 11a).

Extrinsic oxygen vacancies are introduced by variation of the Ga/M ratio to form $RE_3Ga_{5+x}M_{1-x}O_{14-\delta}$ and enable water absorption. The hydration thermodynamics is affected by the size of the M ions, generally becoming more favourable with increasing the size of the cationic radius (enthalpy of hydration reducing from -97 kJ mol^{-1} for M = Si, to -120 kJ mol^{-1} for M = Sn).[179] Calculations demonstrated that protons can adopt different configurations on the three non-equivalent oxygen positions O1, O2, and O3 (Fig. 11b). The lowest energy proton positions are bound to the O3 site, which is shared by the GaO_4 tetrahedra and GaO_6 octahedra.[178] Proton conductivity appears to be anisotropic, with a lower enthalpy of diffusion along the c-axis in the Si langasite, while the ionic migration is easier along the ab plane for the Ta langasite (langatate). The different anisotropy of proton conductivity is due to the different cation ordering for the two compositions.[180]

All the $RE_3Ga_5MO_{14}$ compositions are mixed p-type electronic and ionic conductors at high temperatures due to a minority of electron holes, and pure oxide ion and proton conductors at lower temperatures. The conductivity of these materials is predominantly protonic below 800 °C and in the range $\sim$10^{-6} to 10^{-4} S cm^{-1} between 400 and 800 °C.[178–180] While the proton conductivities of these compounds are lower than conventional perovskite conductors, the langasite structure allows for large compositional variations,[181] thus providing a wide range of langasite-type oxides of which proton conducting properties are mostly unexplored.

The conductivities of gallium-based oxides are among the highest exhibited by oxides containing tetrahedral moieties. Further examples are constituted by reports of proton conductivity in acceptor doped $Gd_{3-x}A_xGaO_6$ (A = Ca, Sr), of which structure is composed by distorted isolated GaO_4 tetrahedra,[182] and in cuspidines of composition $La_4Ga_{2-x}Ti_xO_{9+x/2}$, which present corner-sharing Ga_2O_7 polyhedral units.[183] The Ga^{3+} cation has a strong preference for tetrahedral coordination,[184] with the structures of several gallates containing either isolated tetrahedra or different types of corner-sharing GaO_4 polyhedral units linkages.[185–188] Given the structural variety of these systems, investigation of further gallium-based oxides potentially able to support substantial proton conductivity is warranted.

3.3 Apatite-type oxides

Apatite oxides have general formula $A_{10-x}B_6O_{26\pm\delta}$, where A is a rare-earth metal such as La or an alkaline earth metal such as Sr or Ba, and B is a p-block element such as P, Si or Ge. The apatite structure possesses hexagonal symmetry and is formed by a framework of isolated BO_4 tetrahedra constituting two channels running parallel to the c-axis; the inner channel contains rows of A cations in a ring formation with a row of oxide ions at the centre (Fig. 12a).

Si- and Ge-based lanthanum apatites are known oxide ion conductors thanks to the presence of interstitial oxygen defects which mediate the oxide ion transport.[189,190] These systems are able to absorb significant concentrations of water;[191,192] for example, $\sim$0.75H_2O molecules per formula unit in $La_{9.6}Si_6O_{26.4}$ and $\sim$0.55H_2O molecules in $La_{9.67}Ge_6O_{26.5}$.[193,194] Similarly to the case of Ruddlesden–Popper oxides, water is incorporated on the interstitial oxygen sites.[191,193]

The interstitial sites are close to the centre of the La channel in Si-apatites, forming distorted SiO_5 units,[193] while they are in proximity of the GeO_4 tetrahedra forming Ge_2O_9 units in Ge-apatites (Fig. 12b).[194,195] Water absorption leads to the introduction of protonic defects which are located on the oxide ions at the centre of the La ring, in an arrangement which agrees
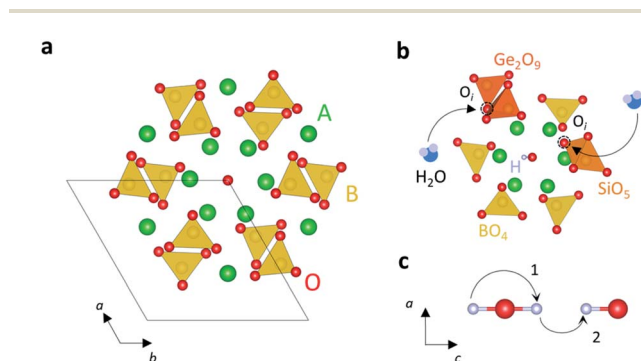

Fig. 12 (a) Crystal structure of apatite $A_{10-x}B_6O_{26\pm\delta}$. (b) Representation of the water absorption mechanism. The interstitial O_i site is close to the centre of the La channel in Si-apatites, and hydration leads to the formation of distorted SiO_5 units. In the Ge-apatite the interstitial site is in proximity of the GeO_4 tetrahedra, with the water absorption resulting in the creation of Ge_2O_9 units. Protons are located on the oxide ion at the centre of the La ring. (c) Schematic of the possible proton transfer mechanism composed by rotation (1) and hopping (2) within the channel parallel to the c-axis.

18846 | J. Mater. Chem. A, 2021, 9, 18836–18856

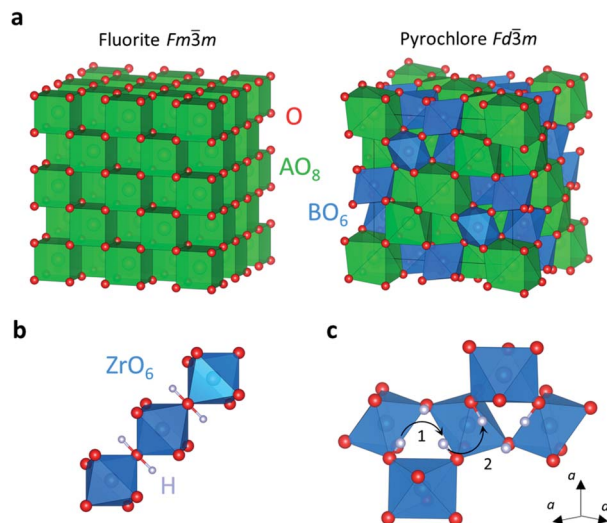This journal is © The Royal Society of Chemistry 2021

Fig. 13 (a) Crystal structure of cubic fluorite and $A_2B_2O_7$ pyrochlore. The fluorite structure is represented with a $2 \times 2 \times 2$ supercell. (b) Calculated most stable proton location in pyrochlore $La_2Zr_2O_7$. The proton is bound to the shared apical oxygen of the corner-sharing ZrO_6 octahedral chains. There are two equivalent proton sites due to the symmetry of the cell. (c) Schematic representation of the long-rage transport pathway composed by proton hopping between adjacent equivalent proton sites (1) and migration towards another closed region (2).

with the one of isostructural hydroxyapatite $(Ca_{10}(PO_4)_6(OH)_2)$ (Fig. 12b).[195]

Despite the large levels of water absorption, the presence of proton conductivity in these apatite oxides is unclear. León-Reina *et al.* reported an increase in the conductivity of $La_{9.75}Ge_6O_{26.62}$ under humidified atmosphere suggesting proton conduction below 400 °C.[196] However, Orera *et al.* argued that the increase in ionic conductivity may be associated with an enhancement of the oxide ion conduction due to the larger concentration of interstitial oxide ions.[191] Preliminary calculations demonstrated that protons are most stable when pointing towards a neighbouring oxide ion in the channel, thus implying that long-range diffusion requires OH rotation before proton transfer (Fig. 12c). However, such rotational motion has a high energy barrier ($\sim$1.5 eV), suggesting that proton diffusion through rotation and hopping within the channel is unfavourable.[195] Further electrical characterisation (*i.e.*, determination of the proton transport number and investigation of the presence of any isotope effect) is required to unambiguously determine whether Si- and Ge-based apatite oxides can support proton conduction.

Isostructural hydroxyapatite materials can support proton conduction, with reports of membrane electrolytes with high proton conductivity ($\sim$10^{-2} S cm^{-1} at 700 °C) and efficient fuel cell applications.[197,198] Moreover, it has been demonstrated that it possible to prepare apatite oxide systems with d^1 cations (Cr^{5+}) showing mixed protonic and electronic conductivity for potential electrode utilisation.[199] Thanks to its large flexibility, the apatite structure allows the accommodation of a wide range of cations and defects which can enable different types of ionic

transports, thus motivating further investigation of oxides crystallising in this structural family.

4. Fluorite-related oxides

Fluorite-based oxides are usually known for their oxide ion conducting properties. Fluorite materials such as yttria stabilised zirconia (YSZ) and doped ceria constitute the most conventional oxide ion conductors thanks to ability of the structure of supporting oxide ion conduction. Some oxide materials having fluorite or fluorite-related superstructures however exhibit significant proton conductivity.

4.1 $A_2B_2O_7$ compounds

Rare-earth oxides with general formula $A_2B_2O_7$ (A = La, Nd, Sm, Er; B = Ti, Zr, Sn, Ce) exhibit proton conductivity.[200–208] These compounds are typically classified as having fully ordered pyrochlore structures or oxygen deficient disordered fluorite-type structures. The pyrochlore structure (space group $Fd\bar{3}m$) is composed by chains of distorted BO_6 octahedra, with the A cations in a distorted 8-fold cubic coordination, while the fluorite structure (space group $Fm\bar{3}m$) can be described by a face-centred cubic arrangement of A cations in a cubic 8-fold coordination (Fig. 13a). The pyrochlore structure is considered as a superstructure of the ideal cubic fluorite, having twice the unit cell parameter and 1/8 of the oxygen sites unoccupied.[209]

The formation of the $A_2B_2O_7$ pyrochlore phase is driven by the tendency for ordering of the cations on the A and B sites. This tendency depends on the relative sizes of the cations: as the difference in cationic sizes increases (*i.e.* the radius of the A-site cation becomes larger), stabilisation of the ordered pyrochlore unit cell is favoured.[204,210,211] The ratio between the ionic radii of the A and B cations (r_A/r_B) can be used as a tolerance factor for describing the formation of one structure over the other.[212] For example, $La_2Zr_2O_7$ adopts the pyrochlore structure,[211] while $La_2Ce_2O_7$ is most often reported as a disordered fluorite.[205] The oxygen vacancies can exhibit short-range ordering or disordering, thus leading to the formation of either pyrochlore-like (in fluorite systems) or fluorite-like (in pyrochlore structures) domains on the local scale.[211,213,214]

Acceptor doping on the A site with alkaline earth cations promotes water incorporation through the introduction of oxygen vacancies.[201,204,208] The hydration is almost independent on the nature of the B site cation but correlates with the size of the rare-earth element, becoming more favourable (enthalpy of hydration more exothermic) on increasing the ionic radius of the RE cation, displaying a trend opposite to $RE_{1-x}A_xMO_4$ materials. For example, the enthalpy of hydration in Ca-doped $A_2Sn_2O_7$ reduces to -44 kJ mol^{-1} for A = Er to -76 kJ mol^{-1} for A = Sm and -103 kJ mol^{-1} for A = La.[215]

The most studied compositions are doped $La_2Zr_2O_7$ and $La_2Ce_2O_7$ thanks to their higher conductivities and larger protonic components. Ca-doped $La_2Zr_2O_7$ has a conductivity of $\sim$10^{-4} S cm^{-1} at 600 °C and a proton transport number of $\sim$1 under wet reducing atmosphere,[201,216–219] while doped $La_2Ce_2O_7$ compounds have conductivity of $\sim$10^{-3} S cm^{-1} at the same

This journal is © The Royal Society of Chemistry 2021

J. Mater. Chem. A, 2021, **9**, 18836–18856 | **18847**
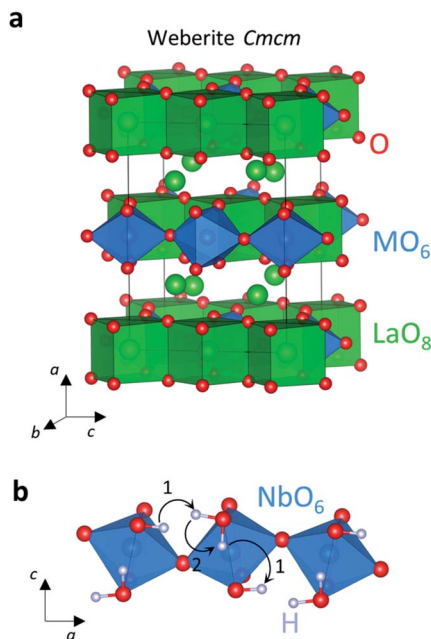
a

Weberite *Cmcm*

b

Fig. 14 (a) Crystal structure of weberite La_3MO_7 composed by chains of corner sharing MO_6 octahedra and edge-sharing LaO_8 cubes. (b) Calculated most stable proton locations in La_3NbO_7 and representation of the lowest energy proton percolation pathway formed by hopping (1) and rotation (2) motion along the non-shared equatorial oxygen atoms of the NbO_6 octahedra.

temperature, albeit with a lower protonic component.[205,220] Contrary to $BaCeO_3$-based perovskites, doped-$A_2Ce_2O_7$ materials exhibit excellent chemical stability in H_2O- and CO_2-containing atmospheres, showing no signs of reaction after exposure at 700 °C for 100 h.[221] These systems are investigated for ammonia synthesis, hydrogen separation membranes and fuel cell applications,[221–223] with peak power densities >700 mW cm^{-2} at 700 °C reported for PCFCs with doped $A_2Ce_2O_7$ electrolytes.[224–226]

Atomistic calculations on pyrochlore $La_2Zr_2O_7$ demonstrated that protons are located on a lowest energy site on the shared apical oxygen of the corner-sharing ZrO_6 octahedral units (Fig. 13b).[227,228] Long-range proton diffusion occurs along the ZrO_6 octahedral network, through an intra-polyhedral migration pathway composed by two separated hopping paths.[228] A proton hops on the edges of the equilateral triangle formed by three adjacent equivalent proton sites and can then migrate towards the next closed region (Fig. 13c). The two paths have very similar migration energies of 0.32 eV and 0.39 eV respectively. A third path corresponding to partial rotation around the oxygen atom has little contribution to the long-range conduction due to its considerable higher energy (0.54 eV).[228] This is in contrast with conventional perovskite conductors, where migration occurs *via* a rotation and hopping mechanism with the rotational step having the lowest energy barrier.[8,229]

4.2 RE$_3$BO$_7$ oxides

Niobates and tantalates of composition RE_3MO_7 (RE = Y, La–Lu; M = Nb, Ta) present mixed electronic, oxide ion and proton

conductivity, with a significant protonic component under wet oxidising conditions.[230–234] The compounds containing the larger lanthanides (RE = La, Gd) generally crystallise with a weberite structure, while the compositions with the smaller lanthanide cations have fluorite, distorted fluorite or pyrochlore structures.[234,235] The weberite structure is an anion deficient fluorite-related superstructure exhibiting different polytype forms.[236] The La_3MO_7 weberite structure (space group *Cmcm* or *Pnma*) can be described as composed by chains of corner-sharing MO_6 octahedra perpendicular to the *b*-axis and edge-sharing distorted LaO_8 cubes (Fig. 14a).[237,238] Similarly to the case of $A_2B_2O_7$ oxides, the Ln_3MO_7 compositions having the fluorite structure exhibit shot-range ordering of the anion vacancies and contain pyrochlore microdomains on the local scale.[239]

In the niobates, the enthalpy of hydration regularly decreases with the radius of the rare-earth cation. The water absorption is favoured for the compounds containing smaller RE^{3+} ions: the water concentration is 2–3% water per formula unit for the compounds with RE = Y, Yb, Lu, while it is considerably lower for La_3NbO_7.[233] Extrinsic oxygen vacancies can be introduced in the weberite lanthanum niobate/tantalate structures *via* acceptor doping. The doped $La_{3-x}A_xMO_{7-x/2}$ (A = Ca, Sr) compositions are stable under oxidising and reducing conditions and exhibit mixed ionic–electronic conductivity with a wide electrolytic domain ($\sim10^{-20}$ to 10^{-5} atm in p_{O2}) and a proton transport number of 0.4 at 600 °C.[230,231] The enthalpies of hydration are in the range -133 kJ mol^{-1} to -117 kJ mol^{-1} and their conductivities are $\sim10^{-4}$ to 10^{-3} S cm^{-1} at 600 °C.[230,231]

Calculations on weberite La_3NbO_7 showed that the most stable proton sites are on the non-shared equatorial oxygen atom of the NbO_6 octahedra (Fig. 14), in contrast with $La_2Zr_2O_7$ where protons are located on the shared apical oxygen.[240] Protons migrate *via* rotational and hopping motion through a long-range lowest energy percolation pathway along the non-shared equatorial oxygen atoms and parallel to the *a*-axis (Fig. 14b). The rotational paths around the non-shared equatorial oxygen atoms have energy barrier of 0.34–0.43 eV, while the intra- and inter-octahedral hoppings have barriers of 0.41–0.54 eV.[240]

The anisotropicity of migration is related to the configuration of the octahedral chains and the preference of protons of residing on the non-shared equatorial oxide ions.[241] The rate-determining step for diffusion is the inter-octahedral hopping between two adjacent non-shared oxygen atoms, which presents the highest energy barrier.[241]

4.3 Lanthanum tungstate oxides

Several lanthanide tungstate oxides with a $\sim3:1$ Ln_2O_3–WO_3 molar ratio (Ln = La, Nd, Gd and Er) have been reported to show predominant proton conduction under humidified atmosphere below 900 °C.[242–247] Lanthanum tungstate oxides in the compositional region 25–30 mol% La_2O_3 have general formula $La_{28-x}W_{4+x}O_{54+3x/2}v_{2-3x/2}$ (v denotes the number of oxygen vacancies) and are also known as $La_{27}W_5O_{55.5-\delta}$, $La_{5.5}WO_{11.25-\delta}$

18848 | *J. Mater. Chem. A*, 2021, **9**, 18836–18856

This journal is © The Royal Society of Chemistry 2021

or La_6WO_{12}. They exhibit proton transport number of ~1 and conductivities of ~10^{-3} S cm^{-1} at 600 °C.[242,244,248] These systems present good stability under CO_2 atmosphere, with no signs of degradation after annealing at 700 °C and 800 °C.[249] La_6WO_{12} is also chemically and mechanically compatible with conventional cathode materials such as $La_{0.7}Sr_{0.3}MnO_{3-\delta}$ (LSM) and $La_{0.75}Sr_{0.25}Cr_{0.5}Mn_{0.5}O_{3-\delta}$ (LSCM) and chromite anode perovskites such as $La_{0.85}Sr_{0.15}Cr_{0.9}Ni_{0.1}O_{3-\delta}$ (LSCN) and $La_{0.75}Ce_{0.1}Sr_{0.15}CrO_{3-\delta}$ (LSCCe), while it reacts with BSCF.[250–253] Fuel cells with La_6WO_{12}-based electrolytes display open circuit voltage (OCV) values close to the theoretical Nernst voltage, although delivering only modest power densities (~50 mW cm^{-2} at 700 °C).[244,251,254] Due to the presence of mixed protonic and electronic conduction at $T > 700$ °C, La_6WO_{12}-based materials have also been investigated for application as high temperature hydrogen separation membranes, which constitute an interesting solution for the recovering of H_2 from low-quality gases.[255] High hydrogen permeability rates >10^{-2} mL min^{-1} cm^{-2} have been obtained for Mo- and Re-substituted La_6WO_{12}-based membranes due to a substantial increase in the electronic conductivity,[256,257] while permeation rates of 0.15 mL min^{-1} cm^{-2} have been reported for dual-phase composite membranes.[258] These values are significantly higher than the typical hydrogen rates of state-of-the-art doped $SrCeO_3$ perovskite membranes (~10^{-3} mL min^{-1} cm^{-2}).[259,260]

$La_{28-x}W_{4+x}O_{54+3x/2}v_{2-3x/2}$ compounds crystallise in an oxygen deficient fluorite-related tetragonal superstructure composed by WO_6 octahedra oriented in alternating directions and with the lanthanum cations in a regular 8-fold cubic coordination (La1) or having a highly distorted 7-fold coordination (La2).[261] Some of the La2 sites are partially occupied by the excess tungsten present in the structure (x), which effectively act a self-dopant creating intrinsic W_{La} substitutional defects.[261,262] The cation disorder is accompanied by large static disorder in the oxygen sub-lattice.[261–265] Characterisation of the hydration and proton conduction mechanisms of these systems is still lacking, probably due to challenges associated in modelling the large anion and cation disorder present in the structure.

Overall, the presence of substantial proton conductivity in oxides having fluorite-related superstructures motivates the investigation of the proton conducting properties of similar structural systems. For example, several bismuth-based oxides having complex fluorite-related superstructures exhibit very high oxide ion conductivities.[266–269] The high ionic conduction is due to the presence of anion disorder and of flexible metal polyhedral units with variable coordination; these structural features could potentially also allow for significant proton transport in these systems.

5. Concluding remarks

This perspective has presented an overview of the most significant types of solid oxide proton conductors beyond cerate and zirconate perovskite oxides. Such compounds belong to different structural families and exhibit a variety of distinct water absorption and proton transport mechanisms. The structural and mechanistic features of hydration and proton conduction were discussed, highlighting the salient differences between these alternative materials and the traditional perovskite oxide conductors. The diverse characteristics of these less established conductors point to new potential crystal routes and can be used to inform the discovery of novel solid oxide proton conductors.

A fundamental prerequisite for proton conduction is the incorporation of protonic defects, which in perovskite oxides (and several other proton conductors) usually occurs via water absorption on the extrinsic oxygen vacancies introduced by acceptor doping. However, the solubility and nature of the dopants limit the oxygen vacancy concentration and influence the degree of hydration.[8,138,270] In this respect, systems with inherently defective lattices such as hexagonal perovskite derivatives with oxygen deficient layers and brownmillerite oxides are particularly interesting, as they can absorb large concentrations of water on the intrinsic oxygen vacancies already present in their structures. This also theoretically eliminates any proton trapping effects caused by donor doping, which are usually detrimental for the overall conductivity of conventional perovskite conductors.[8,42,271]

Proton transport in perovskites and other oxides having extended octahedral networks usually occurs via rotation and hopping of protons along intra-polyhedral pathways. Intra-polyhedral hopping is instead unfavoured in systems containing tetrahedral units, where inter-tetrahedral migration is the common diffusion route. Notably, flexible isolated tetrahedral and variable coordination moieties with high dynamic and rotational mobility enable proton transport. An important aspect that emerges is that the mechanisms of proton transport strongly depend on the coordination environments and the particular topology of the crystal structure. This is in analogy with oxide ion conducting materials,[169,268,272–274] and encourages the exploration of structure types with disordered sub-lattices and/or able to support variable coordination environments. Structure-type oxides with extended tetrahedral networks could also constitute an interesting avenue of research.

Recent reports demonstrating significant proton conductivity in semiconducting oxides,[275] Li-intercalation materials[276,277] and high entropy oxides[278] further expand the explorable chemical and structural space and inspire innovative strategies for the design of novel proton conducting systems. Highly hydrated metastable oxide phases potentially showing high proton conductivity could also be stabilised via high temperature synthesis under humidified atmospheres or with low temperature fabrication processes.[279] As in the case of Li-ion and oxide ion conducting materials,[280,281] computational screening methods could be implemented for selecting candidate solid oxide proton conductors and guide the experimental discovery process.[282] The latter should go hand in hand with a thorough determination of the crystal structure characteristics enabling the desired proton transport properties. Neutron and X-ray diffraction techniques will still have a central role in the characterisation of the average crystal structures and identification of the proton sites, essential pieces of information in order to understand the properties of proton conducting oxides.[283–285] Analysis of the local structural details with total

This journal is © The Royal Society of Chemistry 2021

J. Mater. Chem. A, 2021, 9, 18836–18856 | 18849

scattering (pair distribution function, PDF) methods,[286] X-ray absorption spectroscopy[287] and solid-state NMR[121,176] will be important for the investigation of increasingly complex systems or disordered oxides and to characterise the effects of local order/disorder on the functional properties. The employment of neutron spectroscopy techniques such as inelastic and quasi elastic neutron scattering (INS and QENS), which make use of the contrast given by the large incoherent neutron scattering cross section of the hydrogen atom, will allow to complement the structural studies with the characterisation of the proton dynamics and the diffusional phenomena.[284,288] Further opportunities will arise with the development of advanced sample environments enabling *in situ* studies of materials under operating conditions and with multiple probes. In addition, it is clear how computational techniques and atomistic modelling methods will be complementary to the experimental approach for the comprehensive characterisation of the mechanisms and energetics of protonation and conduction.

Discovery of the next-generation solid oxide proton conductors crucially depends on exploring novel materials and structure types, and on the fundamental understanding of the structure and mechanistic relationships. The latter is of paramount importance for the development of solid proton conducting materials equating or having superior performances to perovskite-based oxides.

Conflicts of interest

There are no conflicts to declare.

Acknowledgements

References

1 I. Staffell, D. Scamman, A. Velazquez Abad, P. Balcombe, P. E. Dodds, P. Ekins, N. Shah and K. R. Ward, *Energy Environ. Sci.*, 2019, **12**, 463–491.
2 S. van Renssen, *Nat. Clim. Change*, 2020, **10**, 799–801.
3 B. C. H. Steele and A. Heinzel, *Nature*, 2001, **414**, 345–352.
4 A. J. Jacobson, *Chem. Mater.*, 2010, **22**, 660–674.
5 E. D. Wachsman and K. T. Lee, *Science*, 2011, **334**, 935–939.
6 M. A. Laguna-Bercero, *J. Power Sources*, 2012, **203**, 4–16.
7 J. B. Hansen, *Faraday Discuss.*, 2015, **182**, 9–48.
8 K. D. Kreuer, *Annu. Rev. Mater. Res.*, 2003, **33**, 333–359.
9 E. C. C. De Souza and R. Muccillo, *Mater. Res.*, 2010, **13**, 385–394.
10 H. Iwahara, T. Esaka, H. Uchida and N. Maeda, *Solid State Ionics*, 1981, **3–4**, 359–363.
11 H. Iwahara, H. Uchida and N. Maeda, *J. Power Sources*, 1982, **7**, 293–301.
12 H. Iwahara, H. Uchida and S. Tanaka, *Solid State Ionics*, 1983, **9–10**, 1021–1025.
13 H. Iwahara, T. Yajima and H. Ushida, *Solid State Ionics*, 1994, **70–71**, 267–271.
14 H. Iwahara, T. Yajima, T. Hibino, K. Ozaki and H. Suzuki, *Solid State Ionics*, 1993, **61**, 65–69.
15 H. Iwahara, *Solid State Ionics*, 1996, **86–88**, 9–15.
16 E. Fabbri, D. Pergolesi and E. Traversa, *Chem. Soc. Rev.*, 2010, **39**, 4355–4369.
17 L. Malavasi, C. A. J. Fisher and M. S. Islam, *Chem. Soc. Rev.*, 2010, **39**, 4370–4387.
18 E. Fabbri, L. Bi, D. Pergolesi and E. Traversa, *Adv. Mater.*, 2012, **24**, 195–208.
19 L. Bi, S. Boulfrad and E. Traversa, *Chem. Soc. Rev.*, 2014, **43**, 8255–8270.
20 N. Kochetova, I. Animitsa, D. Medvedev, A. Demin and P. Tsiakaras, *RSC Adv.*, 2016, **6**, 73222–73268.
21 N. L. R. M. Rashid, A. A. Samat, A. A. Jais, M. R. Somalu, A. Muchtar, N. A. Baharuddin and W. N. R. Wan Isahak, *Ceram. Int.*, 2019, **45**, 6605–6615.
22 C. Duan, J. Huang, N. Sullivan and R. O'Hayre, *Appl. Phys. Rev.*, 2020, **7**, 011314.
23 L. Malavasi, C. Ritter and G. Chiodelli, *Chem. Mater.*, 2008, **20**, 2343–2351.
24 A. K. Eriksson Andersson, S. M. Selbach, T. Grande and C. S. Knee, *Dalton Trans.*, 2015, **44**, 10834–10846.
25 G. C. Mather, G. Heras-Juaristi, C. Ritter, R. O. Fuentes, A. L. Chinelatto, D. Pérez-Coll and U. Amador, *Chem. Mater.*, 2016, **28**, 4292–4299.
26 J. F. Basbus, M. D. Arce, F. R. Napolitano, H. E. Troiani, J. A. Alonso, M. E. Saleta, M. A. González, G. J. Cuello, M. T. Fernández-Díaz, M. P. Sainz, N. Bonanos, C. E. Jimenez, L. Giebeler, S. J. A. Figueroa, A. Caneiro, A. C. Serquis and L. V. Mogni, *ACS Appl. Energy Mater.*, 2020, **3**, 2881–2892.
27 T. Norby, M. Widerøe, R. Glöckner and Y. Larring, *Dalton Trans.*, 2004, 3012–3018.
28 H. Iwahara, T. Yajima and H. Ushida, *Solid State Ionics*, 1994, **70–71**, 267–271.
29 H. Matsumoto, Y. Kawasaki, N. Ito, M. Enoki and T. Ishihara, *Electrochem. Solid-State Lett.*, 2007, **10**, B77–B80.
30 S. Imashuku, T. Uda, Y. Nose, G. Taniguchi, Y. Ito and Y. Awakura, *J. Electrochem. Soc.*, 2009, **156**, B1–B8.
31 D. Han, K. Shinoda, S. Sato, M. Majima and T. Uda, *J. Mater. Chem. A*, 2015, **3**, 1243–1250.
32 E. Gilardi, E. Fabbri, L. Bi, J. L. M. Rupp, T. Lippert, D. Pergolesi and E. Traversa, *J. Phys. Chem. C*, 2017, **121**, 9739–9747.
33 L. Yang, S. Wang, K. Blinn, M. Liu, Z. Liu, Z. Cheng and M. Liu, *Science*, 2009, **326**, 126–129.
34 S. Choi, C. J. Kucharczyk, Y. Liang, X. Zhang, I. Takeuchi, H. Ji and S. M. Haile, *Nat. Energy*, 2018, **3**, 202–210.
35 K. S. Knight, *Solid State Ionics*, 2000, **127**, 43–48.
36 I. Ahmed, C. S. Knee, M. Karlsson, S. -. Eriksson, P. F. Henry, A. Matic, D. Engberg and L. Börjesson, *J. Alloys Compd.*, 2008, **450**, 103–110.
37 L. Mazzei, A. Perrichon, A. Mancini, G. Wahnström, L. Malavasi, S. F. Parker, L. Börjesson and M. Karlsson, *J. Mater. Chem. A*, 2019, **7**, 7360–7372.

38 K. D. Kreuer, T. Dippel, Y. M. Baikov and J. Maier, *Solid State Ionics*, 1996, **86–88**, 613–620.

39 W. Münch, G. Seifert, K. D. Kreuer and J. Maier, *Solid State Ionics*, 1996, **86–88**, 647–652.

40 W. Münch, G. Seifert, K. D. Kreuer and J. Maier, *Solid State Ionics*, 1997, **97**, 39–44.

41 W. Münch, K. D. Kreuer, G. Seifert and J. Maier, *Solid State Ionics*, 2000, **136–137**, 183–189.

42 J. A. Dawson, J. A. Miller and I. Tanaka, *Chem. Mater.*, 2015, **27**, 901–908.

43 W. Suksamai and I. S. Metcalfe, *Solid State Ionics*, 2007, **178**, 627–634.

44 T. Schober and H. G. Bohn, *Solid State Ionics*, 2000, **127**, 351–360.

45 K. Nomura and H. Kageyama, *Solid State Ionics*, 2007, **178**, 661–665.

46 M. Oishi, S. Akoshima, K. Yashiro, K. Sato, J. Mizusaki and T. Kawada, *Solid State Ionics*, 2008, **179**, 2240–2247.

47 D. Han, Y. Noda, T. Onishi, N. Hatada, M. Majima and T. Uda, *Int. J. Hydrogen Energy*, 2016, **41**, 14897–14908.

48 C. Duan, J. Tong, M. Shang, S. Nikodemski, M. Sanders, S. Ricote, A. Almansoori and R. O'Hayre, *Science*, 2015, **349**, 1321–1326.

49 C. Duan, R. J. Kee, H. Zhu, C. Karakaya, Y. Chen, S. Ricote, A. Jarry, E. J. Crumlin, D. Hook, R. Braun, N. P. Sullivan and R. O'Hayre, *Nature*, 2018, **557**, 217–222.

50 H. An, H. Lee, B. Kim, J. Son, K. J. Yoon, H. Kim, D. Shin, H. Ji and J. Lee, *Nat. Energy*, 2018, **3**, 870–875.

51 C. Duan, R. Kee, H. Zhu, N. Sullivan, L. Zhu, L. Bian, D. Jennings and R. O'Hayre, *Nat. Energy*, 2019, **4**, 230–240.

52 S. Choi, T. C. Davenport and S. M. Haile, *Energy Environ. Sci.*, 2019, **12**, 206–215.

53 E. Vøllestad, R. Strandbakke, M. Tarach, D. Catalán-Martínez, M. Fontaine, D. Beeaff, D. R. Clark, J. M. Serra and T. Norby, *Nat. Mater.*, 2019, **18**, 752–759.

54 G. Marnellos and M. Stoukides, *Science*, 1998, **282**, 98–100.

55 K. H. Ryu and S. M. Haile, *Solid State Ionics*, 1999, **125**, 355–367.

56 S. V. Bhide and A. V. Virkar, *J. Electrochem. Soc.*, 1999, **146**, 2038–2044.

57 N. Zakowsky, S. Williamson and J. T. S. Irvine, *Solid State Ionics*, 2005, **176**, 3019–3026.

58 R. Sažinas, C. Bernuy-López, M. Einarsrud and T. Grande, *J. Am. Ceram. Soc.*, 2016, **99**, 3685–3695.

59 R. Sažinas, M. F. Sunding, A. Thøgersen, I. Sakaguchi, T. Norby, T. Grande and J. M. Polfus, *J. Mater. Chem. A*, 2019, **7**, 3848–3856.

60 Y. Yamazaki, R. Hernandez-Sanchez and S. M. Haile, *Chem. Mater.*, 2009, **21**, 2755–2762.

61 D. Pergolesi, E. Fabbri, A. D'Epifanio, E. Di Bartolomeo, A. Tebano, S. Sanna, S. Licoccia, G. Balestrino and E. Traversa, *Nat. Mater.*, 2010, **9**, 846–852.

62 L. Katz and R. Ward, *Inorg. Chem.*, 1964, **3**, 205–211.

63 J. Darriet and M. A. Subramanian, *J. Mater. Chem.*, 1995, **5**, 543–552.

64 L. S. Ramsdell, *Am. Mineral.*, 1947, **32**, 64–82.

65 S. Fop, J. M. S. Skakle, A. C. McLaughlin, P. A. Connor, J. T. S. Irvine, R. I. Smith and E. J. Wildman, *J. Am. Chem. Soc.*, 2016, **138**, 16764–16769.

66 S. Fop, K. S. McCombie, E. J. Wildman, J. M. S. Skakle and A. C. Mclaughlin, *Chem. Commun.*, 2019, **55**, 2127–2137.

67 A. Gilane, S. Fop, F. Sher, R. I. Smith and A. C. Mclaughlin, *J. Mater. Chem. A*, 2020, **8**, 16506–16514.

68 S. Fop, K. S. McCombie, E. J. Wildman, J. M. S. Skakle, J. T. S. Irvine, P. A. Connor, C. Savaniu, C. Ritter and A. C. Mclaughlin, *Nat. Mater.*, 2020, **19**, 752–757.

69 S. Fop, J. A. Dawson, A. D. Fortes, C. Ritter and A. C. McLaughlin, *Chem. Mater.*, 2021, **33**, 4651–4660.

70 M. S. Islam, *Solid State Ionics*, 2002, **154–155**, 75–85.

71 N. Torino, P. F. Henry, C. S. Knee, T. S. Bjørheim, S. M. H. Rahman, E. Suard, C. Giacobbe and S. G. Eriksson, *Dalton Trans.*, 2017, **46**, 8387–8398.

72 T. Murakami, J. R. Hester and M. Yashima, *J. Am. Chem. Soc.*, 2020, **142**, 11653–11657.

73 C. D. Ling, M. Avdeev, R. Kutteh, V. V. Kharton, A. A. Yaremchenko, S. Fialkova, N. Sharma, R. B. Macquart, M. Hoelzel and M. Gutmann, *Chem. Mater.*, 2009, **21**, 3853–3864.

74 C. D. Ling, M. Avdeev, V. V. Kharton, A. A. Yaremchenko, R. B. Macquart and M. Hoelzel, *Chem. Mater.*, 2010, **22**, 532–540.

75 M. T. Dunstan, A. F. Pavan, V. V. Kharton, M. Avdeev, J. A. Kimpton, V. A. Kolotygin, E. V. Tsipis and C. D. Ling, *Solid State Ionics*, 2013, **235**, 1–7.

76 M. T. Dunstan, W. Liu, A. F. Pavan, J. A. Kimpton, C. D. Ling, S. A. Scott, J. S. Dennis and C. P. Grey, *Chem. Mater.*, 2013, **25**, 4881–4891.

77 M. T. Dunstan, F. Blanc, M. Avdeev, G. J. McIntyre, C. P. Grey and C. D. Ling, *Chem. Mater.*, 2013, **25**, 3154–3161.

78 J. Wind, R. A. Mole, D. Yu, M. Avdeev and C. D. Ling, *Chem. Mater.*, 2018, **30**, 4949–4958.

79 C. Tabacaru, A. Aguadero, J. Sanz, A. L. Chinelatto, A. Thursfield, D. Pérez-Coll, I. S. Metcalfe, M. T. Fernandez-Díaz and G. C. Mather, *Solid State Ionics*, 2013, **253**, 239–246.

80 A. L. Chinelatto, K. Boulahya, D. Pérez-Coll, U. Amador, C. Tabacaru, S. Nicholls, M. Hoelzel, D. C. Sinclair and G. C. Mather, *Dalton Trans.*, 2015, **44**, 7643–7653.

81 L. F. K. Unti, E. C. Grzebielucka, A. S. Antonio Chinelatto, G. C. Mather and A. L. Chinelatto, *Ceram. Int.*, 2019, **45**, 5087–5092.

82 N. Tarasova, I. Animitsa, A. Galisheva and D. Korona, *Materials*, 2019, **12**, 1668.

83 N. Tarasova, I. Animitsa and A. Galisheva, *J. Solid State Electrochem.*, 2020, **24**, 1497–1508.

84 N. Tarasova, I. Animitsa, A. Galisheva and V. Pryakhina, *Solid State Sci.*, 2020, **101**, 106121.

85 N. Tarasova, A. Galisheva and I. Animitsa, *Int. J. Hydrogen Energy*, 2021, **46**, 16868–16877.

86 J. R. Tolchard and T. Grande, *Solid State Ionics*, 2007, **178**, 593–599.

This journal is © The Royal Society of Chemistry 2021

J. Mater. Chem. A, 2021, **9**, 18836–18856 | **18851**

87 C. Yang, X. Zhang, H. Zhao, Y. Shen, Z. Du and C. Zhang, *Int. J. Hydrogen Energy*, 2015, **40**, 2800–2807.

88 J. Lyagaeva, D. Medvedev, E. Pikalova, S. Plaksin, A. Brouzgou, A. Demin and P. Tsiakaras, *Int. J. Hydrogen Energy*, 2017, **42**, 1715–1723.

89 J. Dailly, S. Fourcade, A. Largeteau, F. Mauvy, J. C. Grenier and M. Marrony, *Electrochim. Acta*, 2010, **55**, 5847–5853.

90 A. Grimaud, F. Mauvy, J. Marc Bassat, S. Fourcade, M. Marrony and J. Claude Grenier, *J. Mater. Chem.*, 2012, **22**, 16017–16025.

91 Z. Chen, J. Wang, D. Huan, S. Sun, G. Wang, Z. Fu, W. Zhang, X. Zheng, H. Pan, R. Peng and Y. Lu, *J. Power Sources*, 2017, **371**, 41–47.

92 L. Miao, J. Hou, Z. Gong, Z. Jin and W. Liu, *Int. J. Hydrogen Energy*, 2019, **44**, 7531–7537.

93 W. Li, B. Guan, L. Ma, S. Hu, N. Zhang and X. Liu, *J. Mater. Chem. A*, 2018, **6**, 18057–18066.

94 H. Tian, W. Li, L. Ma, T. Yang, B. Guan, W. Shi, T. L. Kalapos and X. Liu, *ACS Appl. Mater. Interfaces*, 2020, **12**, 49574–49585.

95 Z. Wang, W. Yang, S. P. Shafi, L. Bi, Z. Wang, R. Peng, C. Xia, W. Liu and Y. Lu, *J. Mater. Chem. A*, 2015, **3**, 8405–8412.

96 C. Gu, X. Wu, J. Cao, J. Hou, L. Miao, Y. Xia, C. Fu and W. Liu, *Int. J. Hydrogen Energy*, 2020, **45**, 23422–23432.

97 A. P. Tarutin, J. G. Lyagaeva, D. A. Medvedev, L. Bi and A. A. Yaremchenko, *J. Mater. Chem. A*, 2021, **9**, 154–195.

98 A. P. Tarutin, J. G. Lyagaeva, A. S. Farlenkov, A. I. Vylkov and D. M. Medvedev, *Ceram. Int.*, 2019, **45**, 16105–16112.

99 Q. Wang, J. Hou, Y. Fan, X. Xi, J. Li, Y. Lu, G. Huo, L. Shao, X. Fu and J. Luo, *J. Mater. Chem. A*, 2020, **8**, 7704–7712.

100 M. Yashima, M. Enoki, T. Wakita, R. Ali, Y. Matsushita, F. Izumi and T. Ishihara, *J. Am. Chem. Soc.*, 2008, **130**, 2762–2763.

101 L. Troncoso, M. D. Arce, M. T. Fernández-Díaz, L. V. Mogni and J. A. Alonso, *New J. Chem.*, 2019, **43**, 6087–6094.

102 L. Zhang, F. Yao, J. Meng, W. Zhang, H. Wang, X. Liu, J. Meng and H. Zhang, *J. Mater. Chem. A*, 2019, **7**, 18558–18567.

103 M. Chen, Y. Xuan, F. Zhang, L. He, X. Wang, H. Pan, J. Ren and Z. Lin, *Int. J. Hydrogen Energy*, 2020, **45**, 14964–14971.

104 K. Fujii, Y. Esaki, K. Omoto, M. Yashima, A. Hoshikawa, T. Ishigaki and J. R. Hester, *Chem. Mater.*, 2014, **26**, 2488–2491.

105 A. K. Cochrane, M. Telfer, C. A. L. Dixon, W. Zhang, P. S. Halasyamani, E. Bousquet and P. Lightfoot, *Chem. Commun.*, 2016, **52**, 10980–10983.

106 Y. Zhou, M. Shiraiwa, M. Nagao, K. Fujii, I. Tanaka, M. Yashima, L. Baque, J. F. Basbus, L. V. Mogni and S. J. Skinner, *Chem. Mater.*, 2021, **33**, 2139–2146.

107 M. Shiraiwa, T. Kido, K. Fujii and M. Yashima, *J. Mater. Chem. A*, 2021, **9**, 8607–8619.

108 W. Zhang, K. Fujii, E. Niwa, M. Hagihala, T. Kamiyama and M. Yashima, *Nat. Commun.*, 2020, **11**, 1224.

109 K. R. Kendall, C. Navas, J. K. Thomas and H. zur Loye, *Chem. Mater.*, 1996, **8**, 642–649.

110 R. J. Goff, D. Keeble, P. A. Thomas, C. Ritter, F. D. Morrison and P. Lightfoot, *Chem. Mater.*, 2009, **21**, 1296–1302.

111 V. Thangadurai and W. Weppner, *Solid State Ionics*, 2004, **174**, 175–183.

112 J. B. Goodenough, J. E. Ruiz-Diaz and Y. S. Zhen, *Solid State Ionics*, 1990, **44**, 21–31.

113 S. B. Adler, J. A. Reimer, J. Baltisberger and U. Werner, *J. Am. Chem. Soc.*, 1994, **116**, 675–681.

114 G. B. Zhang and D. M. Smyth, *Solid State Ionics*, 1995, **82**, 153–160.

115 J. Jankovic, D. P. Wilkinson and R. Hui, *J. Electrochem. Soc.*, 2011, **158**, B61–B68.

116 T. Schober, J. Friedrich and F. Krug, *Solid State Ionics*, 1997, **99**, 9–13.

117 T. Schober and J. Friedrich, *Solid State Ionics*, 1998, **113–115**, 369–375.

118 V. Jayaraman, A. Magrez, M. Caldes, O. Joubert, F. Taulelle, J. Rodriguez-Carvajal, Y. Piffard and L. Brohan, *Solid State Ionics*, 2004, **170**, 25–32.

119 W. Fischer, G. Reck and T. Schober, *Solid State Ionics*, 1999, **116**, 211–215.

120 J. Martinez, C. E. Mohn, S. Stølen and N. L. Allan, *J. Solid State Chem.*, 2007, **180**, 3388–3392.

121 R. Dervişoğlu, D. S. Middlemiss, F. Blanc, Y. Lee, D. Morgan and C. P. Grey, *Chem. Mater.*, 2015, **27**, 3861–3873.

122 J. Bielecki, S. F. Parker, L. Mazzei, L. Börjesson and M. Karlsson, *J. Mater. Chem. A*, 2016, **4**, 1224–1232.

123 J. Bielecki, S. F. Parker, D. Ekanayake, S. M. H. Rahman, L. Börjesson and M. Karlsson, *J. Mater. Chem. A*, 2014, **2**, 16915–16924.

124 A. Fluri, E. Gilardi, M. Karlsson, V. Roddatis, M. Bettinelli, I. E. Castelli, T. Lippert and D. Pergolesi, *J. Phys. Chem. C*, 2017, **121**, 21797–21805.

125 E. Quarez, S. Noirault, M. T. Caldes and O. Joubert, *J. Power Sources*, 2010, **195**, 1136–1141.

126 J. F. Shin, A. Orera, D. C. Apperley and P. R. Slater, *J. Mater. Chem.*, 2011, **21**, 874–879.

127 J. F. Shin, D. C. Apperley and P. R. Slater, *Chem. Mater.*, 2010, **22**, 5945–5948.

128 X. Li and M. Ihara, *J. Electrochem. Soc.*, 2015, **162**, F927–F938.

129 C. Didier, J. Claridge and M. Rosseinsky, *J. Solid State Chem.*, 2014, **218**, 38–43.

130 C. A. Fuller, Q. Berrod, B. Frick, M. R. Johnson, M. Avdeev, J. S. O. Evans and I. R. Evans, *Chem. Mater.*, 2020, **32**, 4347–4357.

131 N. Lu, P. Zhang, Q. Zhang, R. Qiao, Q. He, H. Li, Y. Wang, J. Guo, D. Zhang, Z. Duan, Z. Li, M. Wang, S. Yang, M. Yan, E. Arenholz, S. Zhou, W. Yang, L. Gu, C. Nan, J. Wu, Y. Tokura and P. Yu, *Nature*, 2017, **546**, 124–128.

132 N. Lu, Y. Wang, S. Qiao, H.-B. Li, Q. He, Z. Li, M. Wang, J. Zhang, S. C. Tsang, J. Guo, S. Yang, J. Zhang, K. Deng, D. Zhang, J. Ma, Y. Wu, J. Zhu, Y. Tokura, C.-W. Nan, J. Wu and P. Yu, e-print arXiv:1811.10802, 2018.

133 M. S. Islam, A. M. Nolan, S. Wang, Q. Bai and Y. Mo, *Chem. Mater.*, 2020, **32**, 5028–5035.

18852 | *J. Mater. Chem. A*, 2021, **9**, 18836–18856

This journal is © The Royal Society of Chemistry 2021

134 B. Scherrer, M. V. F. Schlupp, D. Stender, J. Martynczuk, J. G. Grolig, H. Ma, P. Kocher, T. Lippert, M. Prestat and L. J. Gauckler, *Adv. Funct. Mater.*, 2013, **23**, 1957–1964.

135 W. Paulus, H. Schober, S. Eibl, M. Johnson, T. Berthier, O. Hernandez, M. Ceretti, M. Plazanet, K. Conder and C. Lamberti, *J. Am. Chem. Soc.*, 2008, **130**, 16080–16085.

136 A. Nemudry, M. Weiss, I. Gainutdinov, V. Boldyrev and R. Schöllhorn, *Chem. Mater.*, 1998, **10**, 2403–2411.

137 T. Motohashi, Y. Hirano, Y. Masubuchi, K. Oshima, T. Setoyama and S. Kikkawa, *Chem. Mater.*, 2013, **25**, 372–377.

138 R. Haugsrud and T. Norby, *Nat. Mater.*, 2006, **5**, 193–196.

139 R. Haugsrud and T. Norby, *Solid State Ionics*, 2006, **177**, 1129–1135.

140 R. Haugsrud and T. Norby, *J. Am. Ceram. Soc.*, 2007, **90**, 1116–1121.

141 C. Ferrara, A. Mancini, C. Ritter, L. Malavasi and C. Tealdi, *J. Mater. Chem. A*, 2015, **3**, 22258–22265.

142 M. Huse, A. W. B. Skilbred, M. Karlsson, S. G. Eriksson, T. Norby, R. Haugsrud and C. S. Knee, *J. Solid State Chem.*, 2012, **187**, 27–34.

143 L. Jian and C. M. Wayman, *J. Am. Ceram. Soc.*, 1997, **80**, 803–806.

144 S. W. Arulnesan, P. Kayser, J. A. Kimpton and B. J. Kennedy, *J. Solid State Chem.*, 2019, **277**, 229–239.

145 J. E. Auckett, L. Lopez-Odriozola, S. J. Clark and I. R. Evans, *J. Mater. Chem. A*, 2021, **9**, 4091–4102.

146 T. Mokkelbost, H. L. Lein, P. E. Vullum, R. Holmestad, T. Grande and M. Einarsrud, *Ceram. Int.*, 2009, **35**, 2877–2883.

147 A. D. Brandão, I. Antunes, J. R. Frade, J. Torre, V. V. Kharton and D. P. Fagg, *Chem. Mater.*, 2010, **22**, 6673–6683.

148 S. Wachowski, A. Mielewczyk-Gryń, K. Zagórski, C. Li, P. Jasiński, S. J. Skinner, R. Haugsrud and M. Gazda, *J. Mater. Chem. A*, 2016, **4**, 11696–11707.

149 S. Wachowski, B. Kamecki, P. Winiarz, K. Dzierzgowski, A. Mielewczyk-Gryń and M. Gazda, *Inorg. Chem. Front.*, 2018, **5**, 2157–2166.

150 A. Mielewczyk-Gryń, S. Wachowski, A. Witkowska, K. Dzierzgowski, W. Skubida, K. Świerczek, A. Regoutz, D. J. Payne, S. Hull, H. Zhang, I. Abrahams and M. Gazda, *J. Am. Ceram. Soc.*, 2020, **103**, 6575–6585.

151 A. Kuwabara, R. Haugsrud, S. Stølen and T. Norby, *Phys. Chem. Chem. Phys.*, 2009, **11**, 5550–5553.

152 G. C. Mather, C. A. J. Fisher and M. S. Islam, *Chem. Mater.*, 2010, **22**, 5912–5917.

153 N. Kitamura, K. Amezawa, Y. Tomii, N. Yamamoto and T. Hanada, *Solid State Ionics*, 2004, **175**, 563–567.

154 H. Fjeld, K. Toyoura, R. Haugsrud and T. Norby, *Phys. Chem. Chem. Phys.*, 2010, **12**, 10313–10319.

155 A. Magrasó, M. Fontaine, R. Bredesen, R. Haugsrud and T. Norby, *Solid State Ionics*, 2014, **262**, 382–387.

156 J. R. Tolchard, H. L. Lein and T. Grande, *J. Eur. Ceram. Soc.*, 2009, **29**, 2823–2830.

157 T. Norby and A. Magrasó, *J. Power Sources*, 2015, **282**, 28–33.

158 L. Bi, E. Fabbri and E. Traversa, *Electrochim. Acta*, 2018, **260**, 748–754.

159 M. Huse, T. Norby and R. Haugsrud, *J. Electrochem. Soc.*, 2011, **158**, B857.

160 T. S. Bjørheim, T. Norby and R. Haugsrud, *J. Mater. Chem.*, 2012, **22**, 1652–1661.

161 P. Winiarz, K. Dzierzgowski, A. Mielewczyk-Gryń, M. Gazda and S. Wachowski, *Chem.–Eur. J.*, 2021, **27**, 5393–5398.

162 N. Clavier, R. Podor and N. Dacheux, *J. Eur. Ceram. Soc.*, 2011, **31**, 941–976.

163 K. Toyoura and K. Matsunaga, *J. Phys. Chem. C*, 2013, **117**, 18006–18012.

164 J. Wang, L. Zhou, Y. Wang, J. Xu, X. Yang and X. Kuang, *J. Solid State Chem.*, 2018, **268**, 16–21.

165 X. Yang, A. J. Fernández-Carrión, J. Wang, F. Porcher, F. Fayon, M. Allix and X. Kuang, *Nat. Commun.*, 2018, **9**, 4484.

166 J. Li, F. Pan, S. Geng, C. Lin, L. Palatinus, M. Allix, X. Kuang, J. Lin and J. Sun, *Nat. Commun.*, 2020, **11**, 4751.

167 S. Li, F. Schönberger and P. Slater, *Chem. Commun.*, 2003, 2694–2695.

168 F. Schönberger, E. Kendrick, M. S. Islam and P. R. Slater, *Solid State Ionics*, 2005, **176**, 2951–2953.

169 E. Kendrick, J. Kendrick, K. S. Knight, M. S. Islam and P. R. Slater, *Nat. Mater.*, 2007, **6**, 871–875.

170 M. Coduri, S. Casolo, N. Jalarvo and M. Scavini, *J. Appl. Crystallogr.*, 2019, **52**, 712–721.

171 E. Kendrick, K. S. Knight, M. S. Islam and P. R. Slater, *J. Mater. Chem.*, 2010, **20**, 10412–10416.

172 N. Jalarvo, O. Gourdon, Z. Bi, D. Gout, M. Ohl and M. P. Paranthaman, *Chem. Mater.*, 2013, **25**, 2741–2748.

173 F. Giannici, D. Messana, A. Longo and A. Martorana, *J. Phys. Chem. C*, 2011, **115**, 298–304.

174 E. Kendrick, J. Kendrick, A. Orera, P. Panchmatia, M. S. Islam and P. R. Slater, *Fuel Cells*, 2011, **11**, 38–43.

175 Y. Cheng, J. Balachandran, Z. Bi, C. A. Bridges, M. P. Paranthaman, L. L. Daemen, P. Ganesh and N. Jalarvo, *J. Mater. Chem. A*, 2017, **5**, 15507–15511.

176 G. Kim, J. M. Griffin, F. Blanc, S. M. Haile and C. P. Grey, *J. Am. Chem. Soc.*, 2015, **137**, 3867–3876.

177 K. Toyoura, N. Hatada, Y. Nose, I. Tanaka, K. Matsunaga and T. Uda, *J. Phys. Chem. C*, 2012, **116**, 19117–19124.

178 T. S. Bjørheim, R. Haugsrud and T. Norby, *Solid State Ionics*, 2014, **264**, 76–84.

179 T. S. Bjørheim and R. Haugsrud, *Solid State Ionics*, 2015, **275**, 29–34.

180 T. S. Bjørheim, V. Shanmugappirabu, R. Haugsrud and T. E. Norby, *Solid State Ionics*, 2015, **278**, 275–280.

181 B. V. Mill and Y. V. Pisarevsky, Langasite-type materials: from discovery to present state, *Proceedings of the 2000 IEEE/EIA International Frequency Control Symposium and Exhibition (Cat. No. 00CH37052)*, 2000.

182 A. Iakovleva, A. Chesnaud, I. Animitsa and G. Dezanneau, *Int. J. Hydrogen Energy*, 2016, **41**, 14941–14951.

183 M. C. Martín-Sedeño, D. Marrero-López, E. R. Losilla, L. León-Reina, S. Bruque, P. Núñez and M. A. G. Aranda, *Chem. Mater.*, 2005, **17**, 5989–5998.

184 D. Waroquiers, X. Gonze, G. Rignanese, C. Welker-Nieuwoudt, F. Rosowski, M. Göbel, S. Schenk,

This journal is © The Royal Society of Chemistry 2021

J. Mater. Chem. A, 2021, **9**, 18836–18856 | **18853**

P. Degelmann, R. André, R. Glaum and G. Hautier, *Chem. Mater.*, 2017, **29**, 8346–8360.

185 P. Jiang, W. Gao, R. Cong and T. Yang, *Dalton Trans.*, 2015, **44**, 6069–6074.

186 F. Jiang, P. Jiang, M. Yue, W. Gao, R. Cong and T. Yang, *J. Solid State Chem.*, 2017, **254**, 195–199.

187 J. Yang, P. Jiang, M. Yue, D. Yang, R. Cong, W. Gao and T. Yang, *J. Catal.*, 2017, **345**, 236–244.

188 P. Jiang, F. Jiang, M. Yue, J. Ju, C. Xu, R. Cong and T. Yang, *Angew. Chem., Int. Ed.*, 2019, **58**, 5978–5982.

189 E. Kendrick, M. S. Islam and P. R. Slater, *J. Mater. Chem.*, 2007, **17**, 3104–3111.

190 P. M. Panchmatia, O. Alodia, G. J. Rees, M. E. Smith, J. V. Hanna, P. R. Slater and I. M. Saiful, *Angew. Chem., Int. Ed.*, 2011, **50**, 9328–9333.

191 A. Orera and P. R. Slater, *Solid State Ionics*, 2010, **181**, 110–114.

192 A. Pons, E. Béchade, J. Jouin, M. Colas, P. Geffroy, O. Masson, P. Thomas, I. Kagomiya, T. Asaka, K. Fukuda, A. Slodczyk and P. Colomban, *J. Eur. Ceram. Soc.*, 2017, **37**, 2149–2158.

193 B. J. Corrie, J. F. Shin, S. Hull, K. S. Knight, M. C. Vlachou, J. V. Hanna and P. R. Slater, *Dalton Trans.*, 2016, **45**, 121–133.

194 L. Malavasi, A. Orera, P. R. Slater, P. M. Panchmatia, M. S. Islam and J. Siewenie, *Chem. Commun.*, 2011, **47**, 250–252.

195 P. M. Panchmatia, A. Orera, E. Kendrick, J. V. Hanna, M. E. Smith, P. R. Slater and M. S. Islam, *J. Mater. Chem.*, 2010, **20**, 2766–2772.

196 L. León-Reina, J. M. Porras-Vázquez, E. R. Losilla and M. A. G. Aranda, *J. Solid State Chem.*, 2007, **180**, 1250–1258.

197 K. Yamashita, H. Owada, T. Umegaki, T. Kanazawa and K. Katayama, *Solid State Ionics*, 1990, **40–41**, 918–921.

198 X. Wei and M. Z. Yates, *Chem. Mater.*, 2012, **24**, 1738–1743.

199 Y. Aoki, K. Kikutani, E. Tsuji and H. Habazaki, *ECS Electrochem. Lett.*, 2014, **3**, F61–F64.

200 T. Shimura, M. Komori and H. Iwahara, *Solid State Ionics*, 1996, **86–88**, 685–689.

201 T. Omata, K. Okuda, S. Tsugimoto and S. Otsuka-Matsuo-Yao, *Solid State Ionics*, 1997, **104**, 249–258.

202 K. E. J. Eurenius, E. Ahlberg, I. Ahmed, S. G. Eriksson and C. S. Knee, *Solid State Ionics*, 2010, **181**, 148–153.

203 K. E. J. Eurenius, E. Ahlberg and C. S. Knee, *Solid State Ionics*, 2010, **181**, 1577–1585.

204 K. E. J. Eurenius, E. Ahlberg and C. S. Knee, *Dalton Trans.*, 2011, **40**, 3946–3954.

205 V. Besikiotis, C. S. Knee, I. Ahmed, R. Haugsrud and T. Norby, *Solid State Ionics*, 2012, **228**, 1–7.

206 W. Sun, S. Fang, L. Yan and W. Liu, *Fuel Cells*, 2012, **12**, 457–463.

207 L. Kalland, A. Løken, T. S. Bjørheim, R. Haugsrud and T. Norby, *Solid State Ionics*, 2020, **354**, 115401.

208 Z. Zhong, Y. Jiang, Z. Lian, X. Song and K. Peng, *Ceram. Int.*, 2020, **46**, 12675–12685.

209 M. A. Subramanian, G. Aravamudan and G. V. Subba Rao, *Prog. Solid State Chem.*, 1983, **15**, 55–143.

210 V. Besikiotis, S. Ricote, M. H. Jensen, T. Norby and R. Haugsrud, *Solid State Ionics*, 2012, **229**, 26–32.

211 P. E. R. Blanchard, R. Clements, B. J. Kennedy, C. D. Ling, E. Reynolds, M. Avdeev, A. P. J. Stampfl, Z. Zhang and L. Jang, *Inorg. Chem.*, 2012, **51**, 13237–13244.

212 L. Minervini, R. W. Grimes and K. E. Sickafus, *J. Am. Ceram. Soc.*, 2000, **83**, 1873–1878.

213 L. Kalland and C. E. Mohn, *Phys. Chem. Chem. Phys.*, 2020, **22**, 13930–13941.

214 L. Kalland, S. T. Norberg, J. Kyrklund, S. Hull, S. G. Eriksson, T. Norby, C. E. Mohn and C. S. Knee, *Phys. Chem. Chem. Phys.*, 2016, **18**, 24070–24080.

215 T. S. Bjørheim, V. Besikiotis and R. Haugsrud, *Dalton Trans.*, 2012, **41**, 13343–13351.

216 T. Omata and S. Otsuka-Matsuo-Yao, *J. Electrochem. Soc.*, 2001, **148**, E252–E261.

217 Q. A. Islam, S. Nag and R. N. Basu, *Mater. Res. Bull.*, 2013, **48**, 3103–3107.

218 E. P. Antonova, M. V. Ananyev, A. S. Farlenkov, E. S. Tropin, A. V. Khodimchuk and N. M. Porotnikova, *Russ. J. Electrochem.*, 2017, **53**, 651–657.

219 E. P. Antonova, A. S. Farlenkov, E. S. Tropin, V. A. Eremin, A. V. Khodimchuk and M. V. Ananyev, *Solid State Ionics*, 2017, **306**, 112–117.

220 J. Zamudio-García, L. d. Santos-Gómez, J. M. Porras-Vázquez, E. R. Losilla and D. Marrero-López, *J. Alloys Compd.*, 2020, **816**, 152600.

221 Z. Tao, L. Bi, S. Fang and W. Liu, *J. Power Sources*, 2011, **196**, 5840–5843.

222 J. Wang, Y. Xie, Z. Zhang, R. Liu and Z. Li, *Mater. Res. Bull.*, 2005, **40**, 1294–1302.

223 L. Yan, W. Sun, L. Bi, S. Fang, Z. Tao and W. Liu, *Int. J. Hydrogen Energy*, 2010, **35**, 4508–4511.

224 B. Zhang, K. Wu and K. Peng, *J. Power Sources*, 2018, **399**, 157–165.

225 B. Zhang, Z. Zhong, T. Tu, K. Wu and K. Peng, *J. Power Sources*, 2019, **412**, 631–639.

226 M. Zhang, D. Wang, L. Miao, Z. Jin, K. Dong and W. Liu, *Electrochem. Commun.*, 2021, **126**, 107026.

227 M. E. Björketun, C. S. Knee, B. J. Nyman and G. Wahnström, *Solid State Ionics*, 2008, **178**, 1642–1647.

228 K. Toyoura, A. Nakamura and K. Matsunaga, *J. Phys. Chem. C*, 2015, **119**, 8480–8487.

229 M. A. Gomez, M. A. Griffin, S. Jindal, K. D. Rule and V. R. Cooper, *J. Chem. Phys.*, 2005, **123**, 094703.

230 T. Shimura, Y. Tokiwa and H. Iwahara, *Solid State Ionics*, 2002, **154–155**, 653–658.

231 R. Haugsrud and T. Risberg, *J. Electrochem. Soc.*, 2009, **156**, B425.

232 N. Preux, A. Rolle, C. Merlin, M. Benamira, M. Malys, C. Estournes, A. Rubbens and R. Vannier, *C. R. Chim.*, 2010, **13**, 1351–1358.

233 A. Chesnaud, M. -. Braida, S. Estradé, F. Peiró, A. Tarancón, A. Morata and G. Dezanneau, *J. Eur. Ceram. Soc.*, 2015, **35**, 3051–3061.

18854 | *J. Mater. Chem. A*, 2021, **9**, 18836–18856

This journal is © The Royal Society of Chemistry 2021

234 A. V. Shlyakhtina, K. S. Pigalskiy, D. A. Belov, N. V. Lyskov, E. P. Kharitonova, I. V. Kolbanev, A. B. Borunova, O. K. Karyagina, E. M. Sadovskaya, V. A. Sadykov and N. F. Eremeev, *Dalton Trans.*, 2018, **47**, 2376–2392.

235 T. Subramani and A. Navrotsky, *Inorg. Chem.*, 2019, **58**, 16126–16133.

236 L. Cai and J. C. Nino, *Acta Crystallogr., Sect. B: Struct. Sci.*, 2009, **65**, 269–290.

237 H. J. Rossell, *J. Solid State Chem.*, 1979, **27**, 115–122.

238 A. Kahn-Harari, L. Mazerolles, D. Michel and F. Robert, *J. Solid State Chem.*, 1995, **116**, 103–106.

239 L. López-Conesa, J. M. Rebled, M. H. Chambrier, K. Boulahya, J. M. González-Calbet, M. D. Braida, G. Dezanneau, S. Estradé and F. Peiró, *Fuel Cells*, 2013, **13**, 29–33.

240 K. Kato, K. Toyoura, A. Nakamura and K. Matsunaga, *Solid State Ionics*, 2014, **262**, 472–475.

241 K. Kato, K. Toyoura, A. Nakamura and K. Matsunaga, *J. Phys. Chem. C*, 2014, **118**, 9377–9384.

242 R. Haugsrud, *Solid State Ionics*, 2007, **178**, 555–560.

243 T. Shimura, S. Fujimoto and H. Iwahara, *Solid State Ionics*, 2001, **143**, 117–123.

244 A. Magrasó, *J. Power Sources*, 2013, **240**, 583–588.

245 R. Hancke, A. Magrasó, T. Norby and R. Haugsrud, *Solid State Ionics*, 2013, **231**, 25–29.

246 G. S. Partin, D. V. Korona, A. Y. Neiman and K. G. Belova, *Russ. J. Electrochem.*, 2015, **51**, 381–390.

247 Y. Cao, N. Duan, L. Jian, A. Evans and R. Haugsrud, *J. Am. Ceram. Soc.*, 2016, **99**, 3309–3316.

248 M. Zayas-Rey, L. dos Santos-Gómez, D. Marrero-López, L. León-Reina, J. Canales-Vázquez, M. A. G. Aranda and E. R. Losilla, *Chem. Mater.*, 2013, **25**, 448–456.

249 S. Escolástico, C. Solís and J. M. Serra, *Int. J. Hydrogen Energy*, 2011, **36**, 11946–11954.

250 E. Quarez, K. V. Kravchyk and O. Joubert, *Solid State Ionics*, 2012, **216**, 19–24.

251 C. Solís, L. Navarrete, S. Roitsch and J. M. Serra, *J. Mater. Chem.*, 2012, **22**, 16051–16059.

252 C. Solís, V. B. Vert, M. Balaguer, S. Escolástico, S. Roitsch and J. M. Serra, *ChemSusChem*, 2012, **5**, 2155–2158.

253 M. Balaguer, C. Solís, F. Bozza, N. Bonanos and J. M. Serra, *J. Mater. Chem. A*, 2013, **1**, 3004–3007.

254 M. J. Zayas-Rey, L. dos Santos-Gómez, J. M. Porras-Vázquez, E. R. Losilla and D. Marrero-López, *J. Power Sources*, 2015, **294**, 483–493.

255 S. Escolástico, C. Solís, T. Scherb, G. Schumacher and J. M. Serra, *J. Membr. Sci.*, 2013, **444**, 276–284.

256 M. Amsif, A. Magrasó, D. Marrero-López, J. Ruiz-Morales, J. Canales-Vázquez and P. Núñez, *Chem. Mater.*, 2012, **24**, 3868–3877.

257 S. Escolastico, J. Seeger, S. Roitsch, M. Ivanova, W. A. Meulenberg and J. M. Serra, *ChemSusChem*, 2013, **6**, 1523–1532.

258 S. Escolástico, C. Solís, C. Kjølseth and J. M. Serra, *Energy Environ. Sci.*, 2014, **7**, 3736–3746.

259 X. Qi and Y. S. Lin, *Solid State Ionics*, 2000, **130**, 149–156.

260 S. -. Song, E. D. Wachsman, J. Rhodes, S. E. Dorris and U. Balachandran, *Solid State Ionics*, 2004, **167**, 99–105.

261 A. Magrasó, J. M. Polfus, C. Frontera, J. Canales-Vázquez, L. Kalland, C. H. Hervoches, S. Erdal, R. Hancke, M. S. Islam, T. Norby and R. Haugsrud, *J. Mater. Chem.*, 2012, **22**, 1762–1764.

262 L. Kalland, A. Magrasó, A. Mancini, C. Tealdi and L. Malavasi, *Chem. Mater.*, 2013, **25**, 2378–2384.

263 A. Magrasó, C. H. Hervoches, I. Ahmed, S. Hull, J. Nordström, A. W. B. Skilbred and R. Haugsrud, *J. Mater. Chem. A*, 2013, **1**, 3774–3782.

264 T. Scherb, S. A. J. Kimber, C. Stephan, P. F. Henry, G. Schumacher, S. Escolástico, J. M. Serra, J. Seeger, J. Just, A. H. Hill and J. Banhart, *J. Appl. Crystallogr.*, 2016, **49**, 997–1008.

265 A. Magrasó and C. Frontera, *Dalton Trans.*, 2016, **45**, 3791–3797.

266 R. Punn, A. M. Feteira, D. C. Sinclair and C. Greaves, *J. Am. Chem. Soc.*, 2006, **128**, 15386–15387.

267 C. H. Hervoches and C. Greaves, *J. Mater. Chem.*, 2010, **20**, 6759–6763.

268 X. Kuang, J. L. Payne, M. R. Johnson and I. Radosavljevic Evans, *Angew. Chem., Int. Ed.*, 2012, **51**, 690–694.

269 C. D. Ling, S. Schmid, P. E. R. Blanchard, V. Petříček, G. J. McIntyre, N. Sharma, A. Maljuk, A. A. Yaremchenko, V. V. Kharton, M. Gutmann and R. L. Withers, *J. Am. Chem. Soc.*, 2013, **135**, 6477–6484.

270 A. Kruth and J. T. S. Irvine, *Solid State Ionics*, 2003, **162–163**, 83–91.

271 Y. Yamazaki, F. Blanc, Y. Okuyama, L. Buannic, J. Lucio-Vega, C. P. Grey and S. M. Haile, *Nat. Mater.*, 2013, **12**, 647–651.

272 X. Kuang, M. A. Green, H. Niu, P. Zajdel, C. Dickinson, J. B. Claridge, L. Jantsky and M. J. Rosseinsky, *Nat. Mater.*, 2008, **7**, 498–504.

273 X. Yang, A. J. Fernández-Carrión, J. Wang, F. Porcher, F. Fayon, M. Allix and X. Kuang, *Nat. Commun.*, 2018, **9**, 4484.

274 J. R. Peet, C. A. Fuller, B. Frick, M. Zbiri, A. Piovano, M. R. Johnson and I. R. Evans, *Chem. Mater.*, 2017, **29**, 3020–3028.

275 Y. Zhou, X. Guan, H. Zhou, K. Ramadoss, S. Adam, H. Liu, S. Lee, J. Shi, M. Tsuchiya, D. D. Fong and S. Ramanathan, *Nature*, 2016, **534**, 231–234.

276 R. Lan and S. Tao, *Adv. Energy Mater.*, 2014, **4**, 1301683.

277 T. Wei, L. A. Zhang, Y. Chen, P. Yang and M. Liu, *Chem. Mater.*, 2017, **29**, 1490–1495.

278 M. Gazda, T. Miruszewski, D. Jaworski, A. Mielewczyk-Gryń, W. Skubida, S. Wachowski, P. Winiarz, K. Dzierzgowski, M. Łapiński, I. Szpunar and E. Dzik, *ACS Mater. Lett.*, 2020, **2**, 1315–1321.

279 R. B. Cervera, S. Miyoshi, Y. Oyama, Y. E. Elammari, T. Yagi and S. Yamaguchi, *Chem. Mater.*, 2013, **25**, 1483–1489.

280 L. Kahle, A. Marcolongo and N. Marzari, *Energy Environ. Sci.*, 2020, **13**, 928–948.

281 J. Lee, N. Ohba and R. Asahi, *Chem. Mater.*, 2020, **32**, 1358–1370.

This journal is © The Royal Society of Chemistry 2021

J. Mater. Chem. A, 2021, **9**, 18836–18856 | **18855**

282 P. Wisesa, C. Li, C. Wang and T. Mueller, *RSC Adv.*, 2019, **9**, 31999–32009.

283 F. G. Kinyanjui, S. T. Norberg, I. Ahmed, S. G. Eriksson and S. Hull, *Solid State Ionics*, 2012, **225**, 312–316.

284 M. Karlsson, *Dalton Trans.*, 2013, **42**, 317–329.

285 P. Colomban, *Fuel Cells*, 2013, **13**, 6–18.

286 L. Malavasi, H. Kim and T. Proffen, *J. Appl. Phys.*, 2009, **105**, 123519.

287 K. Amezawa, *Curr. Opin. Electrochem.*, 2020, **21**, 250–256.

288 M. Karlsson, *Phys. Chem. Chem. Phys.*, 2015, **17**, 26–38.

18856 | *J. Mater. Chem. A*, 2021, **9**, 18836–18856

This journal is © The Royal Society of Chemistry 2021